



## Detection of multidecadal oceanic variability by ocean data assimilation in the context of a “perfect” coupled model

S. Zhang,<sup>1</sup> A. Rosati,<sup>1</sup> and M. J. Harrison<sup>1</sup>

Received 30 December 2008; revised 11 August 2009; accepted 4 September 2009; published 16 December 2009.

[1] The impact of oceanic observing systems, external radiative forcings due to greenhouse gas and natural aerosol (GHGNA), and oceanic initial conditions on long time variability of oceanic heat content and salinity is assessed by the assimilation of oceanic “observations” in the context of a “perfect” Intergovernmental Panel on Climate Change Fourth Assessment Report model. According to times and locations at which observations are available, the 20th century expendable bathythermograph (XBT) temperature and 21st century Argo temperature and salinity observations are drawn from a model simulation (set as the “truth”) with historical GHGNA radiative forcings. These model observations are assimilated into another coupled model simulation based on temporally varying or fixed year GHGNA values and different oceanic initial conditions. The degree to which the assimilation recovers the truth variability of oceanic heat content and salinity is an assessment of the impact of each factor on the detection of the oceanic “climate.” Results show that both the 20th century XBT and 21st century Argo observations adequately capture the basin-scale variability of heat content. The Argo salinity observations appear to be necessary to reproduce the North Atlantic thermohaline structure and variability. The addition of historical radiative forcings does not make a significant contribution to the detection skill. The initial conditions spun up by historical GHGNA produce better detection skill than the initial conditions spun up by preindustrial fixed year GHGNA due to reduced assimilation shocks. While the 20th century XBT temperature observations alone capture some basic features of salinity variations of the tropical ocean due to the strong T-S relationship from tropical air-sea interactions, the Argo salinity observations are important for global state estimation, particularly in high latitudes where haline effects on ocean density are greater.

**Citation:** Zhang, S., A. Rosati, and M. J. Harrison (2009), Detection of multidecadal oceanic variability by ocean data assimilation in the context of a “perfect” coupled model, *J. Geophys. Res.*, *114*, C12018, doi:10.1029/2008JC005261.

### 1. Introduction

[2] Uncertainty exists in climate modeling which causes a coupled model to drift away from the real world. The uncertainty includes inadequate measurements of natural and/or anthropogenic forcings and incomplete understanding of their radiative effects, as well as inaccurate numerical implementation for other physical processes [Delworth *et al.*, 2006; Collins *et al.*, 2006]. Ocean observations such as temperature and salinity are generally sparse and insufficient to describe oceanic climate features and variability [e.g., Carton *et al.*, 2000; Forget and Wunsch, 2007]. A more accurate assessment for oceanic climate can be achieved by combining coupled model dynamics with observational data.

[3] Coupled data assimilation uses the dynamics of a coupled general circulation model (CGCM) to extract information from observations to reconstruct a time series of climate states. The reconstructed time series is an estimate for how the climate varied in the past. Diagnostics based on the reconstructed products help further understanding for the mechanisms of climate variations, such as the impact of anthropogenic and natural forcings on climate change. Also, the estimate for the present climate state may serve as the initial conditions for a coupled model to predict how the climate will vary in the future.

[4] The quality of an assimilation product is influenced by model bias, assimilation methodology and representation of an observing system. Model bias may create artifacts that can contaminate the assimilation-generated variability and thus is a serious obstacle to obtain a reliable representation of climate variability by combining model and data [Dee and da Silva, 1998; Dee, 2005; Balmaseda *et al.*, 2007]. This study addresses the impact of observing systems, external radiative forcings and initial conditions on the detection of long time variability of oceanic heat content

<sup>1</sup>Geophysical Fluid Dynamics Laboratory, Princeton University, Princeton, New Jersey, USA.

and salinity. As a first step, a perfect model study framework, i.e., “twin” experiment in which “observations” are produced by a model simulation, is used to exclude the model bias issue. To meet the needs of state estimation and forecast initialization, taking the probabilistic nature of climate evolution into account, the NOAA’s Geophysical Fluid Dynamical Laboratory (GFDL) has developed an ensemble coupled data assimilation (ECDA) system using its second generation CGCM (CM2) [Delworth *et al.*, 2006] with an ensemble filter [Anderson, 2003]. Based on the proof-of-concept study [Zhang *et al.*, 2007] for ECDA, this study applies the ECDA system to a series of oceanic data assimilation experiments in the perfect model context to address the following: (1) Are the 20th century temperature and 21st century temperature and salinity observations sufficed to capture the multidecadal variability of oceanic heat content and salinity? (2) What is the impact of external radiative forcings on oceanic state estimation? (3) What is the impact of oceanic initial conditions on decadal time scales?

[5] After describing the methodology in section 2, section 3 analyzes the impact of the observing systems, radiative forcings and initial conditions on the detection of heat content variability. Section 4 discusses the impact of each factor on the detection of salinity variability. The detectability of the North Atlantic thermohaline structure is analyzed and discussed in section 5. Finally, conclusions and discussions are given in section 6.

## 2. Methodology

### 2.1. A Fully CGCM

[6] The coupled model used in this study is a B grid [Wyman, 1996] finite difference atmospheric model (AM2/LM2) [Geophysical Fluid Dynamics Laboratory Global Atmospheric Model Development Team, 2004] coupled with the fourth version of Modular Ocean Model (MOM4) [Griffies *et al.*, 2005]. This is one of two GFDL Intergovernmental Panel on Climate Change Fourth Assessment Report (IPCC AR4) models, called CM2.0 [Randall *et al.*, 2007]. The atmosphere model has 24 vertical levels and  $2.5^\circ$  longitude by  $2^\circ$  latitude horizontal resolution. The physics package includes a K profile planetary boundary layer [Lock *et al.*, 2000], relaxed Arakawa-Schubert convection [Moorthi and Suarez, 1992] and a simple local parameterization of the vertical momentum transport by cumulus convection. The ocean model is configured with 50 vertical levels, 22 levels having uniform 10 m thickness in the top 220 m, and  $1^\circ \times 1^\circ$  horizontal resolution telescoping to  $1/3^\circ$  meridional spacing near the equator. The model has an explicit free surface with a freshwater flux exchange between the atmosphere and ocean. Parameterized physical processes include K profile parameterization vertical mixing, neutral physics, a spatially dependent anisotropic viscosity, and a shortwave radiative penetration depth that depends on a prescribed climatological ocean color. Insolation varies diurnally and the wind stress at the ocean surface is computed using the velocity of the wind relative to the surface currents. An efficient time-stepping scheme [Griffies, 2005] is employed. More details are given by Gnanadesikan *et al.* [2006] and Griffies *et al.* [2005]. The Sea Ice Simulator in the coupled model is a dynamical ice

model with three vertical layers (one for snow and two for ice) and five ice thickness categories. The elastic-viscous-plastic technique [Hunke and Dukowicz, 1997] is used to calculate ice internal stress, and the thermodynamics is a modified Semtner three-layer scheme [Winton, 2000]. The coupled components of this model interact with each other through exchanged fluxes (Figure 1a).

### 2.2. Assimilation Scheme: A Coupled Ensemble Filter

[7] A detailed description of the ensemble coupled data assimilation (ECDA) system using an ensemble filter are given by Zhang *et al.* [2007]. Here we only need to comment on a few aspects of particular relevance to the climate detection addressed in this study.

[8] In this study we address how well the oceanic climate variations can be retrieved by combining oceanic observations with coupled dynamics within the ECDA framework illustrated in Figure 1a. The ensemble filter solves for a temporally varying joint probability distribution function (joint PDF) of coupled state variables in a straight forward manner, in terms of a discrete representation of PDF by finite-size ensemble members. Oceanic data assimilation (ODA) in the coupled framework is carried out by the filtering (Figure 1b) that combines the PDF of an oceanic observation and a prior PDF derived from the coupled model to compute an analysis PDF. The filtering process is implemented by a multivariate linear regression [Anderson, 2003]. The data-adjusted ensemble members are the realizations of the analysis PDF and serve as the initial conditions for the next ensemble integration. The coupled ensemble filter has the following advantages over traditional data assimilation approaches for the particular interests of this study:

[9] 1. The multivariate data assimilation using cross covariances evaluated by the ensemble model integrations helps maintain more consistent physical balance (local T-S relationship, for instance) as observations are incorporated into the model.

[10] 2. The temporally varying error covariances evaluated instantaneously by the ensemble of state variables are fully flow dependent and anisotropic.

[11] 3. The filtering adjusts the joint PDF only up to the second-order moment so that the nonlinearity in long time evolution of oceanic circulations, characterized by higher-order moments, is sustained as schematically illustrated by Figure 1b.

[12] 4. The ECDA filter allows for dynamical coupling among the atmosphere/ocean/land/sea ice components in the assimilation. Whenever a variable in an individual model component is adjusted by the assimilation of observations, instantaneously exchanging fluxes among coupled model components alter more or less the variables in other model components. In this case, the ocean observing system provides constrained sea surface temperatures (SSTs) to the atmosphere thereby impacting surface heat and momentum flux feedbacks. Estimated covariances between, for instance, wind stress and SST are also used to constrain the fluxes in a dynamically consistent fashion. Thus, the generated coupled states may minimize coupling shocks for the next model integration which help enhance the signal-to-noise ratio in the assimilation although allowing

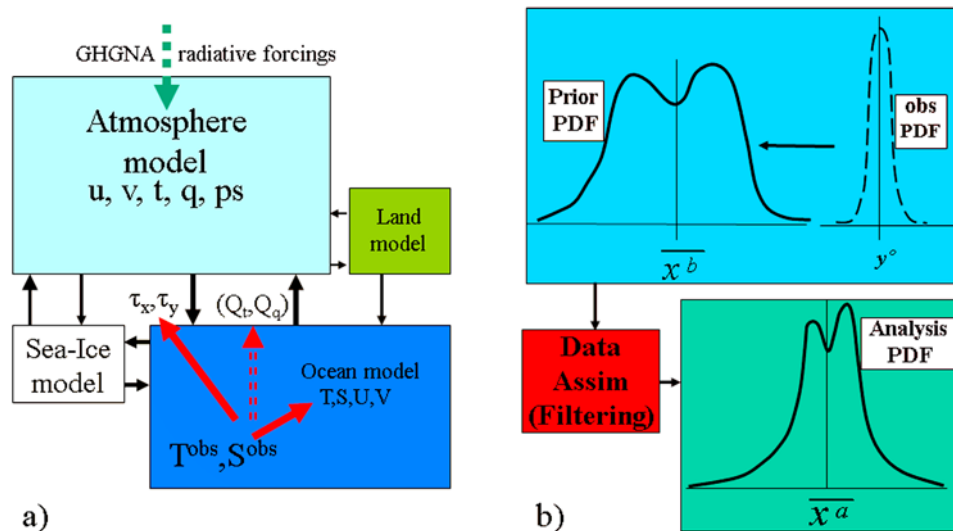


**Figure 1.** Cartoon of how (a) the components in the GFDL atmosphere/ocean/land/sea ice coupled model interact with each other by exchanging fluxes (black arrows) and (b) an ensemble filter updates the probability distribution for a scalar variable given an observation. The dashed green arrow in Figure 1a denotes the radiative forcings expressed by the atmospheric greenhouse gas and natural aerosol (GHGNA) and means that the GHGNA radiative forcings in assimilation may be set as a preindustrial fixed year (1860). The red arrows in Figure 1a indicate that oceanic observations are allowed to impact all oceanic state variables, including the wind stresses at the sea surface. The upper left of Figure 1b represents the prior distribution derived from model ensemble integrations starting from the previous assimilation results. The upper right of Figure 1b represents an observational distribution (usually Gaussian). A filtering process (lower left in Figure 1b) combines the observational and prior distributions to form an analyzed distribution (lower right in Figure 1b) realized by a set of ensemble members, which are initial conditions for the next ensemble integrations.

some uncertainty of surface fluxes that are only constrained by ODA-generated SSTs.

### 2.3. Experimental Design

[13] Figure 2 shows the variability of North Atlantic (NA) temperature and salinity in two model simulations to illustrate the nature of the climate variability this study attempts to address. The variations of monthly mean temperature versus salinity over the upper (200–1000 m; Figures 2a and 2c) and lower (1000–5000 m; Figures 2b and 2d) North Atlantic Ocean (20–70°N) are taken from the GFDL IPCC AR4 “control” and “20th century historical” (called  $h_1$ ) simulations [Randall *et al.*, 2007]. Both the control and historical simulations start from the same initial conditions (marked by a red star), a 300 year spin-up integration initialized from the previous integration [Stouffer *et al.*, 2004]. The control run refers to a 141 year integration with the 1860 fixed year greenhouse gas and natural aerosol (GHGNA) value while the historical simulation uses the temporally varying GHGNA records from 1861 to 2000. It is shown that after around 40 years (black dots in Figure 2) the preindustrial fixed year control run begins to drift away from the historical simulation (each color represents a quarter of the 20th century, e.g., the first quarter is cyan, the last quarter is red, and so on) in both upper and lower portions of the North Atlantic Ocean. In particular, while the upper ocean temperature and salinity of the historical simulation exhibits a clear warming and saltier trend, without the constraint of temporally varying radiative forcings, the control run varies only within a relatively small

range. Here we ask: Do the 20th century expendable bathythermograph (XBT) or 21st century Argo observing network provide sufficient information to capture the trends depicted in Figures 2c and 2d? What follows outlines the observing system simulation experiments used in this study for the climate detection.

[14] As with Zhang *et al.* [2007], the monthly mean data of 25 year (1976–2000 of the model calendar) oceanic/atmospheric/land/sea ice state variables produced by the IPCC  $h_1$  integration serve as the “truth” states. The daily oceanic temperature or temperature and salinity of the truth are projected onto the locations (longitudes, latitudes and depths) and times according to the following two oceanic observing systems:

[15] 1. The 20th century XBT temperature profiles are taken from the World Ocean Database maintained by National Oceanographic Data Center. The profile types are largely the same as used by Levitus *et al.* [2005] for the World Ocean Analysis (WOA), mainly from XBT, but also including CTD (conductivity-temperature-depth), DRB (drifting buoy), OSD (ocean station data), UOR (Undulating Oceanographic Recorder), and MRB (moored buoy). XBTs are the largest single source of oceanic temperature data, being distributed primarily along commercial shipping routes, and thus the spatial coverage is inhomogeneous and particularly sparse in the Arctic and Southern Oceans [see Zhang *et al.*, 2007, Figure 4]. Following Figure 4 of Zhang *et al.* [2007], here we only show the horizontal locations of the profiles deeper than 500 (Figures 3a and 3c) and 1000 (Figures 3b and 3d) m for January 1986 (Figures 3a

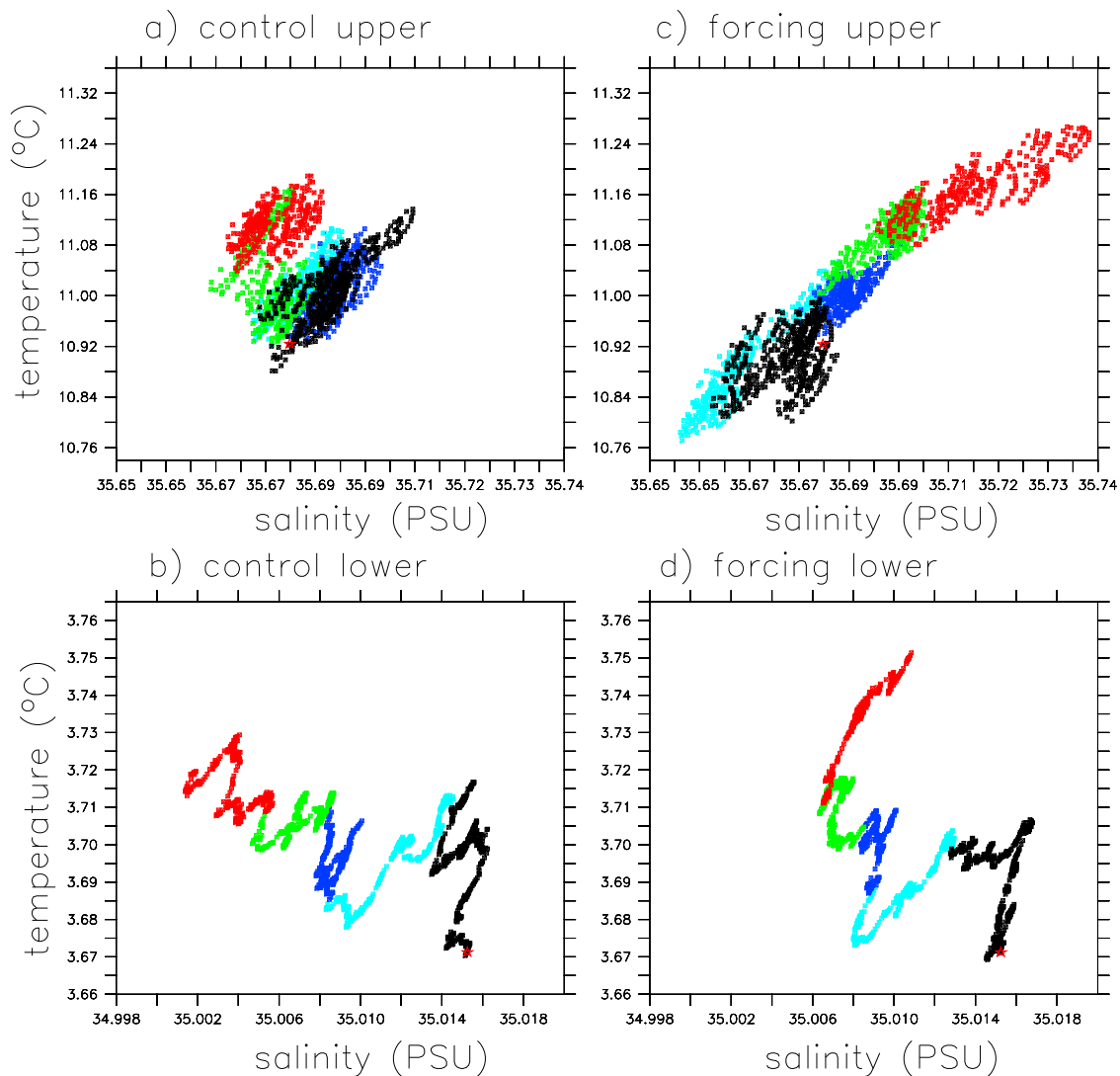


**Figure 2.** The domain-averaged temperature and salinity over the North Atlantic ( $20^{\circ}\text{N}$ – $70^{\circ}\text{N}$ ) (a and c) upper (200–1000 m) and (b and d) lower (1000–5000 m) oceans in T-S space for the control run using the preindustrial (1860) fixed year radiative forcings (Figures 2a and 2b) and the 20th century historical run using the temporally varying radiative forcings (Figures 2c and 2d). The first 40 years are marked by black dots, and each quarter afterward is marked by cyan, blue, green, and red dots, respectively.

and 3b) and 1991 (Figures 3c and 3d). Compared to Figure 4 of Zhang *et al.* [2007], there is a dramatic drop in the number of profiles with depth, for example, only one third of profiles below 500 m, and less than one thirtieth below 1000 m. Most of the XBT profiles only reach 500 m while the profiles below 1000 m are mainly provided by CTDs. Since salinity data (only in CTDs and OSDs) are so sparse, only temperature data in the 20th century network are used in this study.

[16] 2. The 21st century Argo profiles include both temperature and salinity observations, taken from the WOA data set. Here the 2005 Argo network (see the January’s temperature and salinity locations in Figure 4) is repeatedly used to simulate the evolution of the 21st century Argo observations. Unlike the 20th century XBT, the 21st century Argo has a nearly uniform spatial coverage, especially for the Southern Hemisphere where the coverage of

observations is much better than that of the 20th century XBT. In addition, the number of the profiles provided by the Argo Network does not decrease by depth significantly (Figure 4).

[17] The sampling process is basically a trilinear interpolation, added by white noise to simulate random observational errors [Zhang *et al.*, 2007]. The standard deviation of the white noise is  $0.5^{\circ}\text{C}$  for temperature and 0.1 psu for salinity at the sea surface and exponentially decays to zero by 2000 m. Once the model observations are ready, the following two types of GHGNA radiative forcings and oceanic initial conditions are used to conduct a series of assimilation experiments:

### 2.3.1. Temporally Varying Versus Preindustrial Fixed Year GHGNA Radiative Forcings

[18] For a coupled atmosphere/ocean/land/sea ice system, the GHGNA radiative effect serves as the utmost external

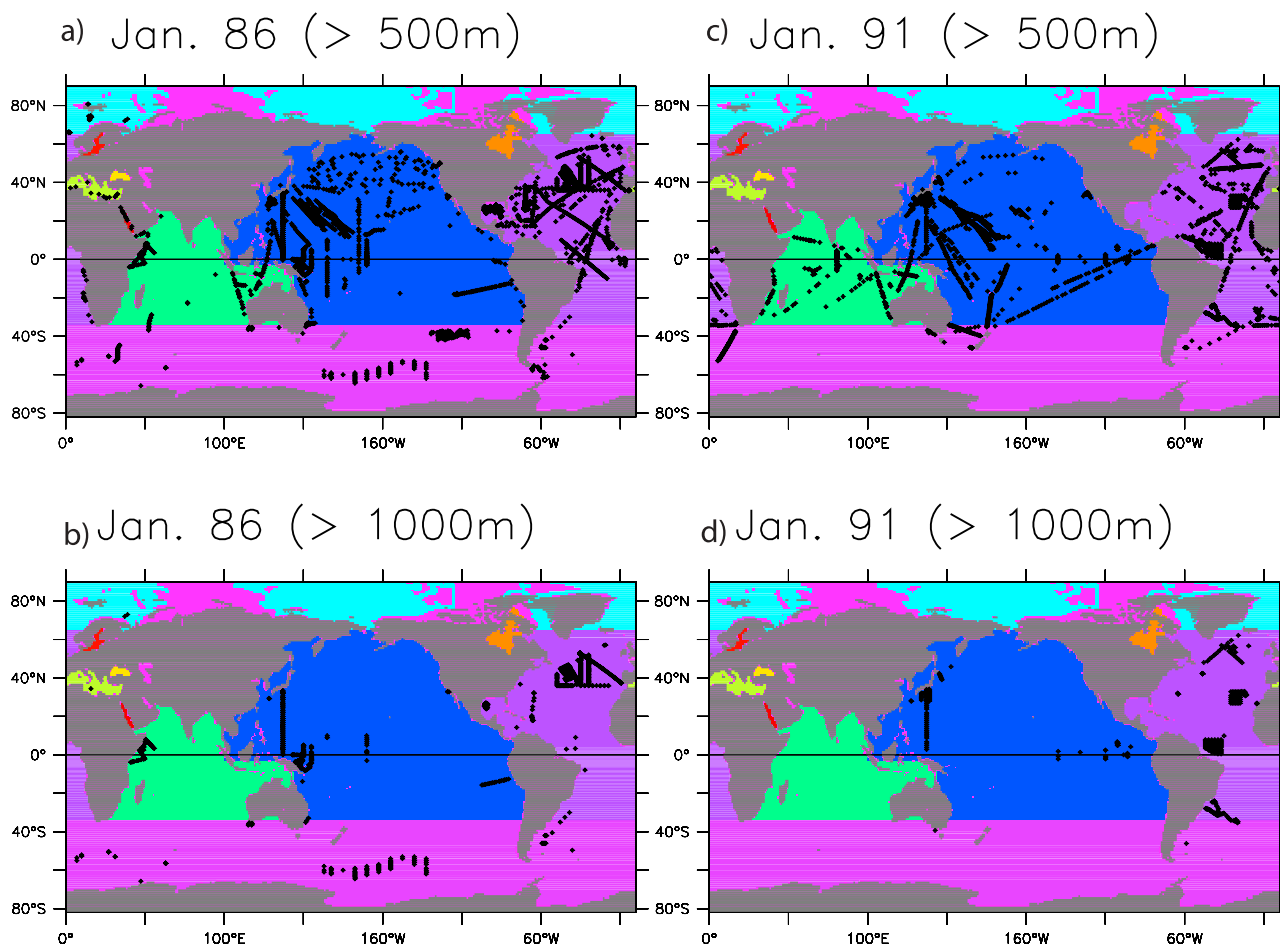


**Figure 3.** Samples of vertical variations of the 20th century oceanic observing network. The locations of observational profiles deeper than (a and c) 500 and (b and d) 1000 m in January 1986 (Figures 3a and 3b) and 1991 (Figures 3c and 3d). The background colors show the individual ocean basins that are examined in this study, the same as used by Zhang *et al.* [2007] following Levitus *et al.* [2000, 2005].

forcing. Previous studies have shown that GHGNA radiative effects are directly responsible for a global scale warming trend [e.g., Manabe, 1979; Manabe and Stouffer, 1979]. The question here is: how important are the historical GHGNA radiative forcings for detecting oceanic variability by assimilating oceanic observations into a coupled model? This question can be answered by performing identical assimilation experiments with the temporally varying or 1860 fixed year GHGNA radiative forcings.

### 2.3.2. Forced (1861–1975) Versus Control (Preindustrial) Oceanic Initial Conditions

[19] The ensemble coupled initial conditions (ICs) in this study are formed by imposing the atmospheric (including land) states at 00UTC 1 January of consecutive years on the oceanic (including sea ice) state that is centered on these years. The control ICs are taken from the IPCC control simulation described at the beginning of this section (a 141 year model integration using the preindustrial (1860) fixed year GHGNA value). The forced ICs are taken from another set of the IPCC historical simulation (called  $h_3$ ) which uses the same temporally varying GHGNA radiative forcings as  $h_1$  but starts from a different initial state (380 year spin-up integration rather than the 300 year of  $h_1$ ). Since the forced and control ICs are taken from the model simulations

driven by different GHGNA radiative forcings beyond 100 years, their oceanic states (especially for deep ocean) are expected to be different. Then how the different oceanic initial conditions from which an assimilation starts influence the assimilation quality?

[20] The assimilation experiments are summarized in Table 1. It is worth mentioning that to justify the ensemble size used in the ensemble assimilation, the assimilation qualities using 6, 12, and 24 member ensembles during a 5 year test period are compared. No significant improvement is found from a 12 member ensemble to a 24 member ensemble. Based on this result, a 12 member ensemble is used for all assimilation experiments.

## 3. Detection of Heat Content Variability

### 3.1. Impact of GHGNA Radiative Forcings

[21] This section examines the impact of external radiative forcings on the detection of heat content variability by analyzing and comparing the assimilation results from ODA<sub>000</sub> and ODA<sub>100</sub>. Both assimilations are based on the 20th century XBT observing network and start from the control ICs but ODA<sub>000</sub> uses the 1860 fixed year GHGNA

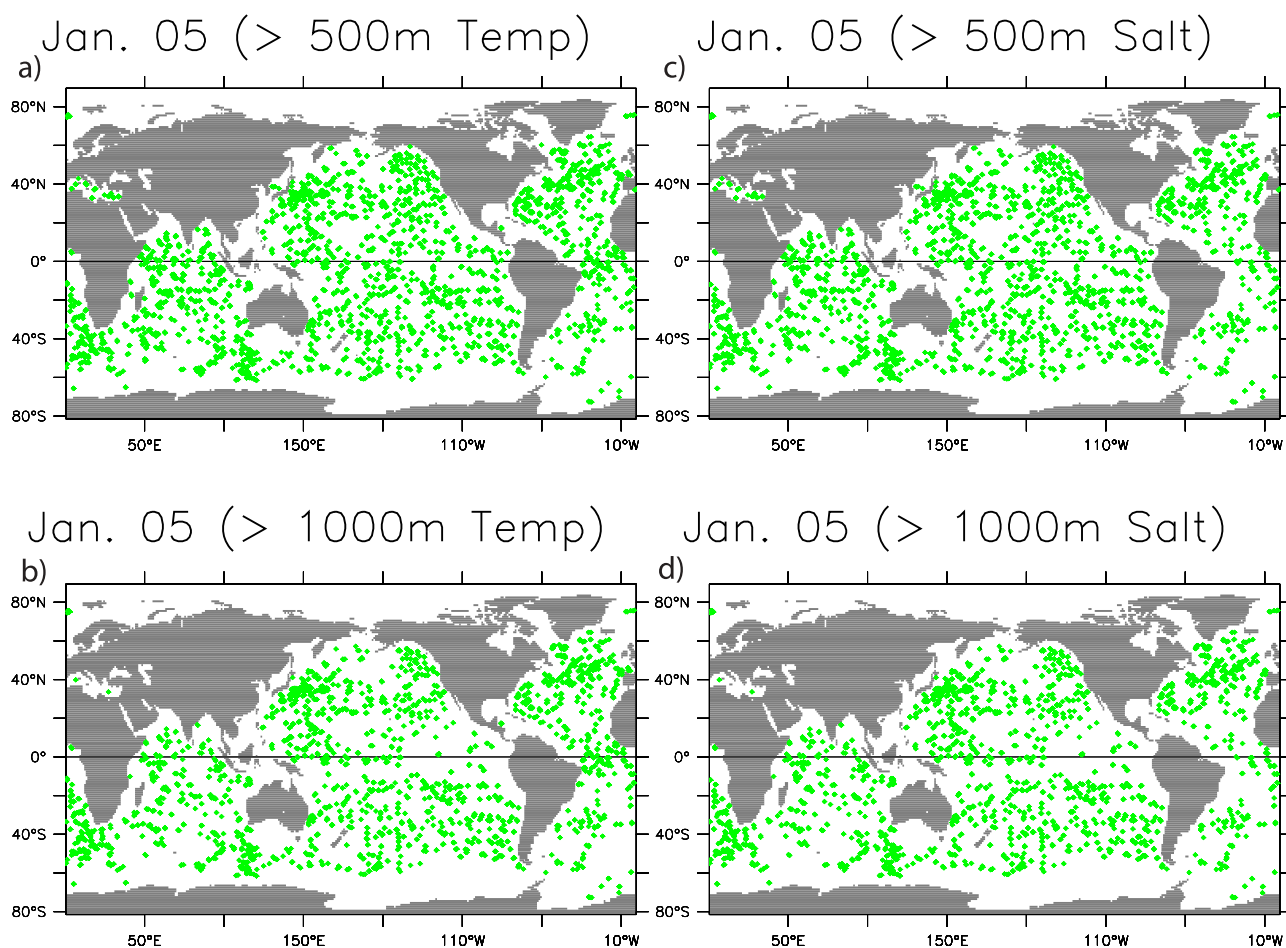


**Figure 4.** Samples of vertical variations of the 21st century oceanic observing network (Argo). The locations of Argo (a and b) temperature and (c and d) salinity profiles deeper than 500 (Figures 4a and 4c) and 1000 (Figures 4b and 4d) m in January 2005.

value while  $ODA_{100}$  uses the historical (temporally varying) GHGNA records (see Table 1).

[22] Time series of heat content (the averaged potential temperature anomaly) over the top 700 m produced by  $ODA_{000}$  and  $ODA_{100}$  are plotted in Figure 5 (dashed red and solid red lines, respectively). The corresponding time series of two free model simulations,  $NOAssim_{00}$  and the truth, are also plotted (dashed green and black lines, respectively) for the validation of assimilation. The heat content of the truth shows a warming trend in all basins but with different rate (the weakest in the Arctic and the strongest in the Indian Ocean) while no apparent trend is

observed in  $NOAssim_{00}$ . The World Ocean heat content in the truth shows a warming trend of  $0.2^{\circ}\text{C}$  over the two and half decades with two interruptions corresponding to the volcanic activities during the early 1980s and 1990s.

[23] After a few years of assimilation spin-up, the decadal variability and multidecadal trend of heat content in all basins and the World Ocean are retrieved well by both  $ODA_{000}$  and  $ODA_{100}$ . Except for the Southern Ocean, Arctic Ocean and North Indian Ocean, the interannual variability of heat content in all other basins is well reproduced in both assimilations. The 20 year averaged root-mean-square (RMS) and mean errors (Table 2) are

**Table 1.** Four Assimilation Experiments and Three Model Simulations

Acronym of Experiments	Description of Experiments	GHGNA Records	Initial Conditions	Observing System
Truth	Model simulation	Temporally varying	Forced from 300 year spin-up	–
$NOAssim_{00}$	Model simulation	Preindustrial fixed year	Preindustrial control	–
$NOAssim_{11}$	Model simulation	Temporally varying	Forced from 380 year spin-up	–
$ODA_{000}$	Oceanic data assimilation	Preindustrial fixed year	Preindustrial control	The 20th century XBT
$ODA_{100}$	Oceanic data assimilation	Temporally varying	Preindustrial control	The 20th century XBT
$ODA_{110}$	Oceanic data assimilation	Temporally varying	Forced from 380 year spin-up	The 20th century XBT
$ODA_{111}$	Oceanic data assimilation	Temporally varying	Forced from 380 year spin-up	The 21st century Argo

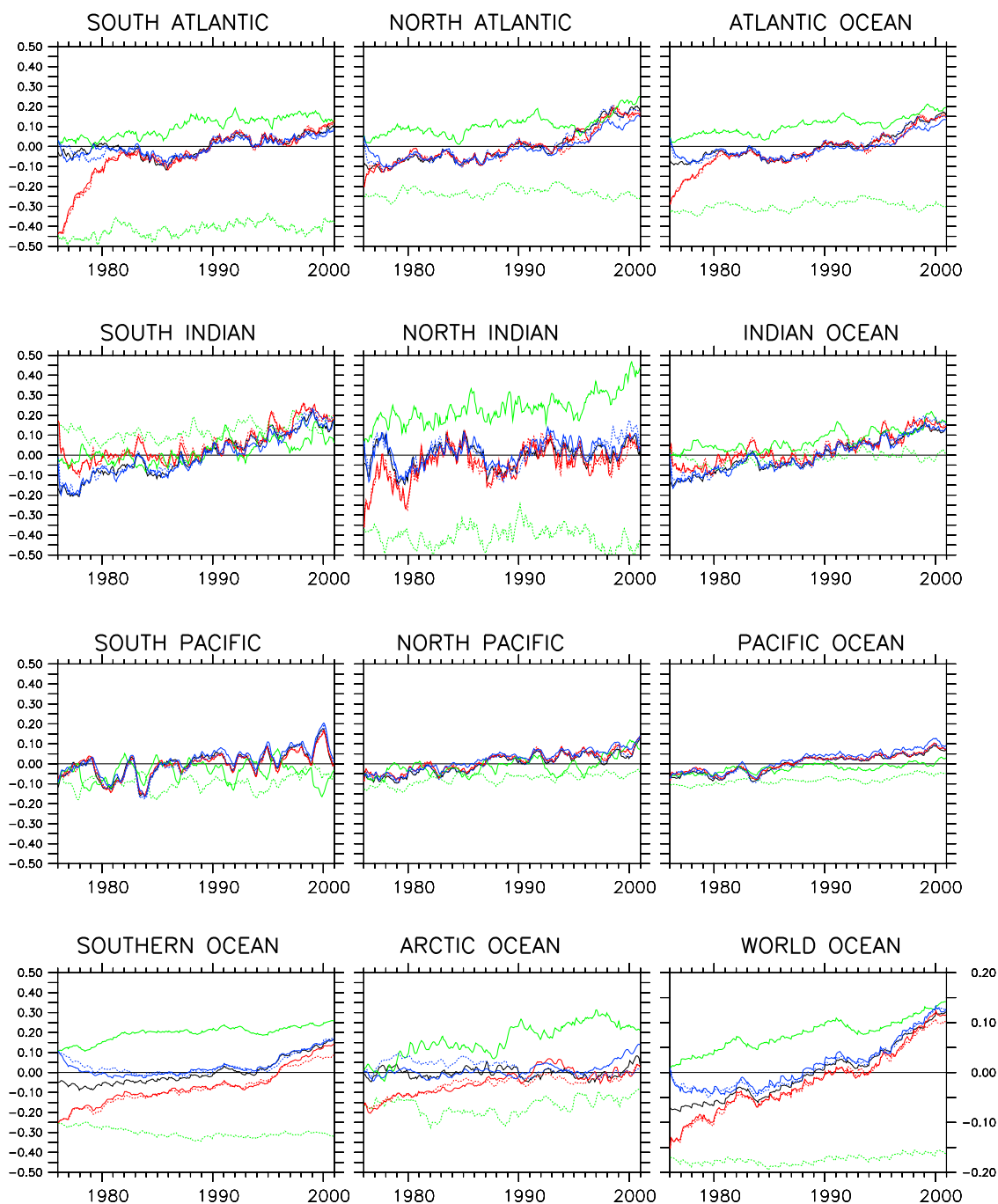


**Figure 5.** Time series of the domain-averaged oceanic temperature anomalies over the top 700 m for individual ocean basins and the World Ocean in the three free model simulations and four ODA experiments (see section 2.3). One of the free model simulations, the GFDL IPCC historical simulation (plotted by black lines) is sampled by the 20th century or 21st century oceanic observing system to form “observations” for ODA and serves as the “truth” of four assimilations: ODA<sub>000</sub> (dashed red line), ODA<sub>100</sub> (solid red line), ODA<sub>110</sub> (dashed blue line), and ODA<sub>111</sub> (solid blue line; see Table 1 for detailed descriptions). Other two free model simulations, NOAssim<sub>00</sub> and NOAssim<sub>11</sub>, are plotted by the dashed and solid green lines, respectively, as the reference of assimilation evaluation.

dramatically reduced through both assimilations from NOAssim<sub>00</sub> (compare the ODA<sub>000</sub> and ODA<sub>100</sub> columns to the NOAssim<sub>00</sub> column). Table 2 also shows that the assimilation skill (for both ODA<sub>000</sub> and ODA<sub>100</sub>) has a basin dependence. The best assimilation skill is from the North Pacific Ocean (the RMS error is reduced by around

70% from NOAssim<sub>00</sub>) and the worst assimilation skill is from the North Indian Ocean (the RMS error is reduced by around 15%). The intermediate assimilation quality is observed in the Southern Ocean and Arctic Ocean, i.e., 30–40% RMS error reduction from NOAssim<sub>00</sub>. The basin dependence of assimilation quality can basically be

**Table 2.** RMS Errors of Oceanic Temperature Over the Top 700 m During the Last 20 Years in Two Model Simulations and Four Assimilation Experiments<sup>a</sup>

Basin	NOAssim <sub>00</sub>	NOAssim <sub>11</sub>	ODA <sub>000</sub>	ODA <sub>100</sub>	ODA <sub>110</sub>	ODA <sub>111</sub>
SAT	0.62(−41)	0.60(11)	0.22/65(0.1)	0.21/5(−0.1)	0.19/10(0.2)	0.19/0(−0.03)
NAT	0.84(−25)	1.0(10)	0.33/61(−1)	0.34/−3(−0.2)	0.28/18(0.2)	0.34/−26(−2)
AT	0.77(−31)	0.91(10)	0.30/61(−0.6)	0.30/0(−0.2)	0.25/17(0.2)	0.29/−16(−1)
SIN	0.66(9)	0.69(−0.6)	0.38/42(4)	0.38/0(4)	0.26/32(0.6)	0.20/30(−0.9)
NIN	0.69(−41)	0.70(24)	0.58/16(−2)	0.60/−3(−2)	0.38/37(1)	0.28/33(2)
IN	0.68(−4)	0.70(6)	0.45/34(3)	0.45/0(2)	0.30/33(0.8)	0.23/23(−0.1)
SPC	0.55(−10)	0.64(−4)	0.17/69(−0.4)	0.16/6(−0.6)	0.15/6(−0.3)	0.19/−26(2)
NPC	0.90(−8)	0.86(−2)	0.22/76(1)	0.22/0(1)	0.17/23(0.1)	0.25/−47(2)
PC	0.78(−9)	0.78(−3)	0.21/73(0.5)	0.20/5(0.3)	0.16/20(−0.1)	0.23/−44(2)
SO	0.53(−33)	0.64(20)	0.33/38(−7)	0.31/6(−6)	0.28/10(2)	0.18/36(2)
AO	0.53(−17)	0.63(19)	0.33/38(−4)	0.38/−15(−3)	0.29/24(2)	0.25/14(2)
WO	0.71(−19)	0.77(7)	0.31/56(−2)	0.31/0(−1)	0.24/23(0.7)	0.24/0(1)

<sup>a</sup>RMS error of oceanic temperature is given in °C. The RMS's reduction (%) of an assimilation from the case to which it is compared (for ODA<sub>000</sub> the RMS's reduction is from NOAssim<sub>00</sub>, for ODA<sub>100</sub> the reduction is from ODA<sub>000</sub>, for ODA<sub>110</sub> the reduction is from ODA<sub>100</sub>, and for ODA<sub>111</sub> the reduction is from ODA<sub>110</sub>). The corresponding mean errors (10<sup>−2</sup> °C) are listed in parentheses. SAT, South Atlantic Ocean; NAT, North Atlantic Ocean; AT, Atlantic Ocean; SIN, South Indian Ocean; NIN, North Indian Ocean; IN, Indian Ocean; SPC, South Pacific Ocean; NPC, North Pacific Ocean; PC, Pacific Ocean; SO, Southern Ocean; AO, Arctic Ocean; WO, World Ocean.

explained by the data coverage in each basin [AchutaRao *et al.*, 2006]. However some interesting points can be drawn from the assimilation performance in the Southern Ocean, Arctic Ocean and North Indian Ocean.

[24] The equilibrium of the oceanic state in ODA is a balance between data adjustment and dynamical constraint. The dynamical constraint here includes (1) the interaction of oceanic circulations in different ocean basins, (2) the structure of local oceanic circulations, and (3) the interaction of coupled components through exchanged fluxes. Usually, when data adjustment produces a local change in the temperature and/or salinity field, the dynamical constraint spreads out the information by these dynamical processes. Thus, although there is a sparse data coverage in the Southern Ocean and Arctic Ocean, the heat content of these 2 Oceans still gradually approaches toward the truth, as a dynamical response of the model to the data constraints of neighboring oceans. In particular, the dynamical constraints here include the interaction of the circulations between the Southern Ocean and the other neighboring oceans such as the South Pacific and Atlantic Oceans as well as the ice-water interactions and ice-atmosphere flux exchanges in the Arctic. Since the ODA's spin-up time in a basin is strongly associated with its observation density [Zhang *et al.*, 2007], the assimilation adjustment in these two Oceans is the slowest.

[25] Associated with the relatively sparse data coverage in the Indian Ocean of the 20th century XBT, a noticeable difference between the assimilation and the truth heat content can be distinguished in the basin. Due to the decrease of data by depth (see Figures 3a and 3b) the assimilation errors increase in the deep ocean, especially in the regions where data becomes very sparse or nonexistent, for example, the North Indian Ocean (see Figure 6a). In particular, the rich spectrum of active circulations driven by the Indian monsoon in the North Indian Ocean and heat and salt exchanges between the Indian and Pacific Oceans by the through flows over the Indonesian archipelagos make more difficulties for ODA to resolve the subannual variability in that region. As a contrast, due to relatively dense data coverage and strong dynamical constraint from interior circulations in the Pacific and Atlantic Oceans, the

heat content of these Oceans is retrieved by the assimilations well from the interannual variability to multidecadal trend down to 2000 m (see Figure 7 for examples).

[26] Comparing the assimilation results of ODA<sub>000</sub> and ODA<sub>100</sub>, we found that the variability of heat content is almost indistinguishable between ODA<sub>000</sub> and ODA<sub>100</sub> in all individual basins and the World Ocean. Quantitative error statistics (Table 2) show both assimilations reduce the heat content RMS errors for the World Ocean at the same rate (56%) from NOAssim<sub>00</sub>. For all individual basins, the difference of the RMS error reduction between ODA<sub>000</sub> and ODA<sub>100</sub> is very small too. From these results, we can conclude that the assimilation with the fixed year or temporally varying GHGNA radiative forcings produces overall equivalent assimilation quality. Based on the study of Deser and Phillips [2009] on the relative roles of the GHGNA radiative forcings and SST in driving the atmospheric circulations, our results here suggest that changes in ocean heat content driven by the radiative forcing changes can be efficiently retrieved by assimilating observed ocean temperature data into the model, which presumably contain sufficient radiative forcing information from air-sea interaction in the past.

[27] The spatial distribution of decadal scale heat content tendency in ODA<sub>000</sub> (Figure 8c) and ODA<sub>100</sub> (Figure 8d) supports the above conclusion. However, ODA<sub>100</sub> produces a colder tendency over the Labrador Sea and a warmer tendency over the Greenland Sea compared to ODA<sub>000</sub>. The phenomenon that “perfect” radiative forcings increase errors in the Labrador Sea and Greenland Sea demonstrates the model's sensitivity in these regions. To understand the mechanism behind this sensitivity requires further studies and shall be addressed in follow-up studies.

### 3.2. Impact of Oceanic Initial Conditions

[28] Holding the setting of ODA<sub>100</sub> but starting the assimilation from the forced ICs, we perform ODA<sub>110</sub> (dashed blue lines in Figure 5). The corresponding model simulation starting from the forced ICs is NOAssim<sub>11</sub> (solid green lines in Figure 5). Almost in all ocean basins (except for the South Indian Ocean) and the World Ocean, NOAssim<sub>11</sub> is much warmer and closer to the truth than NOAssim<sub>00</sub>

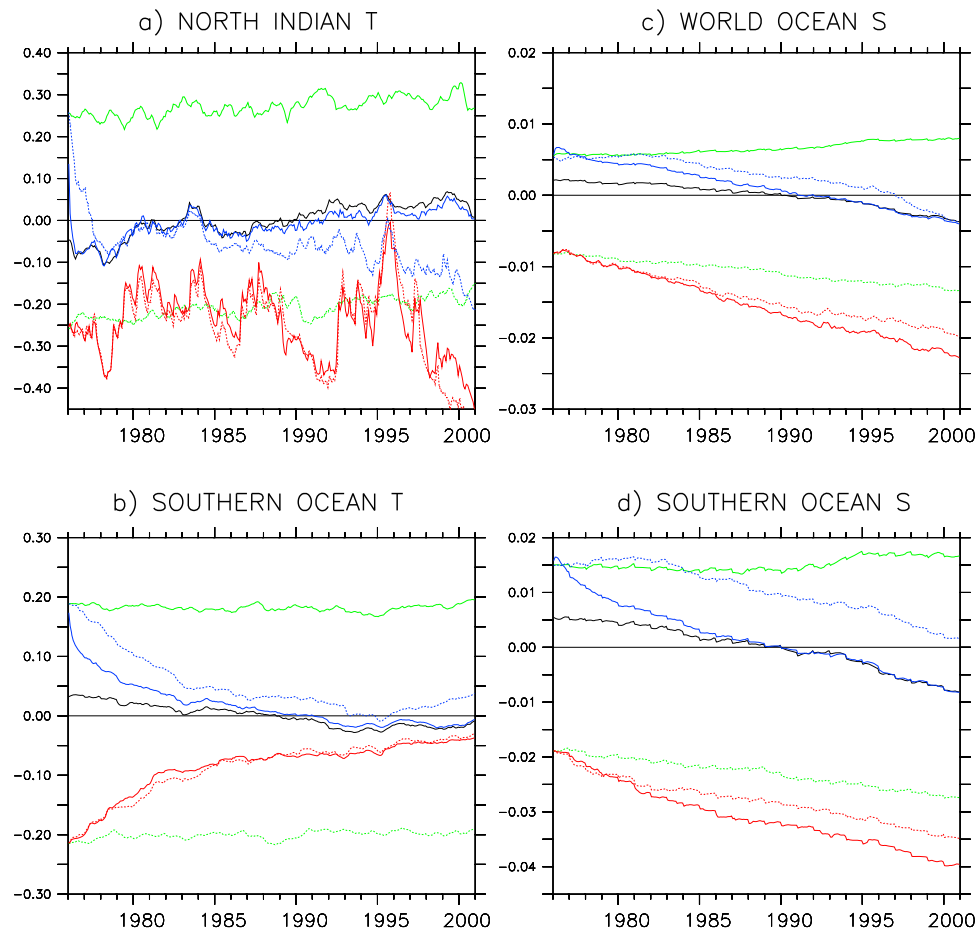


**Figure 6.** Time series of the domain-averaged oceanic (a and b) temperature and (c and d) salinity anomalies of the 700–2000 m for the North Indian Ocean (Figure 6a), the Southern Ocean (Figures 6b and 6d), and the world Ocean (Figure 6c). Otherwise the same as Figure 5.

(dashed green lines). The different initial shocks in the forced and control ICs produce a different assimilation quality for ODA<sub>100</sub> and ODA<sub>110</sub>.

[29] The truth (black) basically lies between NOAssim<sub>00</sub> and NOAssim<sub>11</sub> for most of the basins and the World Ocean. Thus, the NOAssim<sub>00</sub>'s mean error is negative while the NOAssim<sub>11</sub>'s mean error is positive (the NOAssim<sub>00</sub> and NOAssim<sub>11</sub> columns in Table 2). The warmer/colder bias in the forced/control ICs results in the ODA<sub>110</sub>/ODA<sub>100</sub> assimilation approaching the truth from a different side and eventually producing a warmer/colder assimilation bias (compare dashed blue lines to solid red lines in Figure 5; compare the ODA<sub>100</sub> column to the ODA<sub>110</sub> column in Table 2). After the spin-up of a few years, both assimilations appear to capture the interannual variability and decadal trend of heat content in all basins and the World Ocean consistently. However, the quantitative error statistics (Table 2) show that the use of the forced ICs dramatically improves the assimilation quality (compare the ODA<sub>100</sub> and ODA<sub>110</sub> columns). In fact, from ODA<sub>100</sub>, ODA<sub>110</sub> reduces 15–20% of the temperature RMS errors for the Atlantic and Pacific Oceans, 40% for the Indian Ocean and 25% for the World Ocean. The greatest improvement is found in the North Indian Ocean.

[30] The great improvement of the assimilation quality from ODA<sub>100</sub> to ODA<sub>110</sub> can be explained by the small

assimilation shocks in deep ocean produced by the forced oceanic ICs. To recover the  $h_1$  simulation that is driven out by the temporally varying radiative forcings, the forced oceanic ICs that have been spun up over a century by the temporally varying radiative forcings are expected to produce smaller initial shocks in ODA<sub>110</sub> than the control ICs do in ODA<sub>100</sub>. Given too few XBT observations available in deep ocean and the low-frequency nature of deep ocean circulations, the different deep ocean states in the forced and control ICs would make a quite different assimilation quality in the 25 year assimilation.

[31] The greatest improvement from ODA<sub>100</sub> to ODA<sub>110</sub> over the North Indian Ocean is interesting. From the analyses and discussions in section 3.2, we know that the equilibrium of ODA is a balance of data adjustment and dynamical constraint. Confined by continents, the North Indian Ocean lacks large-scale interior circulations like subtropical and subpolar gyres in the Pacific and Atlantic Oceans. Instead, the variability of the North Indian Ocean is mainly driven by the Indian monsoon system and influenced by the adjacent/marginal seas through heat and salt exchanges. Lacking strong interior dynamical constraint, the ODA equilibrium in the North Indian Ocean is mainly determined by the data adjustment and sea surface forcings. Comparing the surface forcings and SSTs in ODA<sub>100</sub> and ODA<sub>110</sub>, we found that the errors of both the wind stress

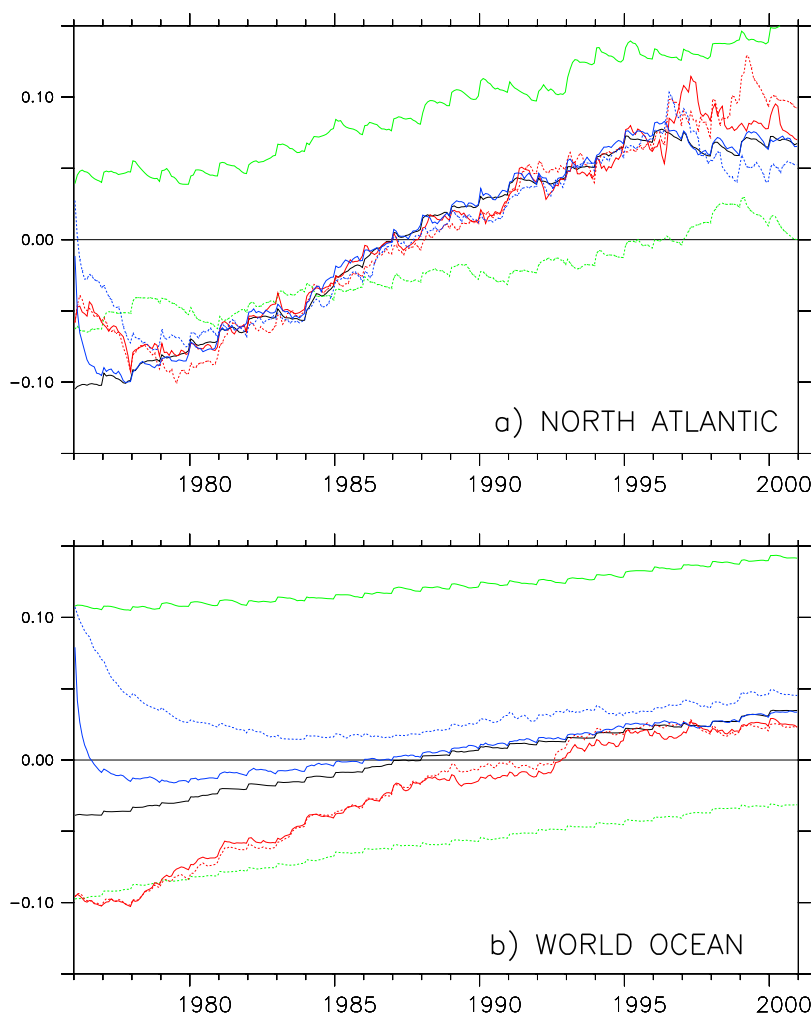


**Figure 7.** Time series of the domain-averaged oceanic temperature anomalies of the 700–2000 m for (a) the North Atlantic Ocean and (b) the World Ocean. Otherwise the same as Figure 5.

and SSTs in  $ODA_{110}$  are much smaller than the ones in  $ODA_{100}$  in the North Indian region. This perhaps suggests that the coupled initial conditions forced by long time GHGNA records make easier for the strong air-sea feedbacks in the North Indian region, which may improve the assimilation skill there, but needs further studies.

[32] The big difference of the 2 decade time tendency of heat content in  $ODA_{100}$  and  $ODA_{110}$  (compare Figure 8e to Figure 8d) is found in the Southern Ocean and the North Atlantic Ocean, especially in deep oceans (not shown). In the Southern Ocean  $ODA_{110}$  has a weaker warming trend but  $ODA_{100}$  has a stronger warming trend. This is associated with the warmer/colder initial states from which  $ODA_{110}/ODA_{100}$  starts (see the solid/dashed green lines in Figure 6b). The difference of time tendency errors over the Labrador Sea and Greenland Sea between  $ODA_{100}$  and  $ODA_{110}$  demonstrates that the decadal variability of the heat content of the sub-Arctic and North Atlantic Oceans, especially for the deep oceans, are sensitive to the oceanic initial conditions. Again, due to the existence of deep convections in the North Atlantic Ocean which is related to heat and salt transport, ice-water interactions and other complex processes, further study is required to assess this sensitivity. The above analyses show that the oceanic initial

conditions that are sufficiently spun up by the temporally varying radiative forcings may help ODA improve the estimate of heat content variability.

### 3.3. Impact of Oceanic Observing Systems

[33] The 21st century Argo network shows the following two substantial differences from the 20th century XBT: (1) The Argo has almost the same number of salinity profiles as temperature (see Figures 4a and 4b). (2) Argo floats are initially deployed on a  $3^\circ \times 3^\circ$  mesh system globally down to 2000 m. Thus, the 21st century Argo provides a much more regularly distributed network than the 20th century XBT.

[34] Replacing the XBT network in  $ODA_{110}$  by the Argo network, we perform assimilation experiment  $ODA_{111}$  (solid blue lines in Figures 5, 6a, and 6b, the  $ODA_{111}$  column in Table 2). From  $ODA_{110}$  to  $ODA_{111}$ , the systematic improvement for the assimilation skill of heat content appears in the whole upper 2000 m. For the top 700 m, a noticeable improvement is found in the Southern Ocean (the RMS error is reduced by 36%), the Indian Ocean (23%) and the Arctic Ocean (14%), while the assimilation skills in the Atlantic and Pacific Oceans appear to drop marginally. As pointed out by AchutaRao *et al.* [2006], the sampling

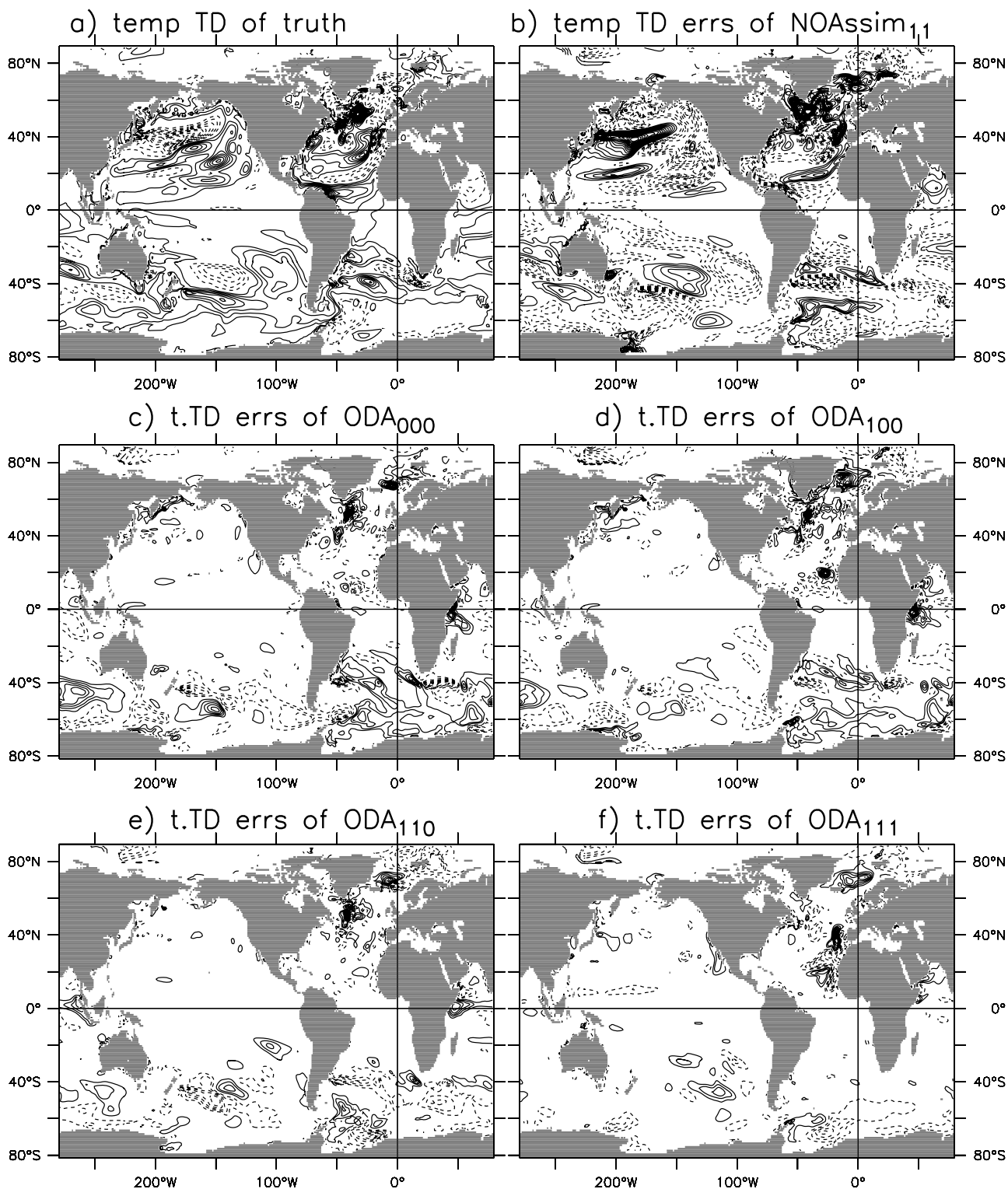


**Figure 8.** (a) Time tendency of the 1980s to the 1990s of the top 700 m ocean temperature in the truth, and the assimilation errors of the time tendency in (c) ODA<sub>000</sub>, (d) ODA<sub>100</sub>, (e) ODA<sub>110</sub>, and (f) ODA<sub>111</sub>. (b) The error of a control case, NOAssim<sub>11</sub>, is also exhibited as a reference for assimilation evaluation. The contour interval is 0.1°C, the zero line is omitted, and the dashed contours are negative.

coverage has a large impact on the inferred temperature variability. Relative to the XBT network, the Argo network improves the coverage of temperature observations at high latitudes (especially for the Southern Hemisphere) and deep

oceans greatly. For the top (say, top 500 m) Pacific and Atlantic Oceans (especially for the North Pacific and Atlantic) the XBT [Zhang *et al.*, 2007, Figure 4] is better than the Argo (Figure 4). The greatest improvement of the

heat content over the top 2000 m is found in the Southern Ocean (the RMS error is reduced by 44%) and the next is in the Indian Ocean (30%) and the Arctic Ocean (17%). Again, these regions are better sampled by Argo. Consequently, the World Ocean's RMS and mean errors of the top 2000 m are improved by 20% and 60%, respectively, by using the 21st century Argo network.

[35] The improvement of the assimilation quality on heat content from ODA<sub>110</sub> to ODA<sub>111</sub> is partly from the Argo salinity observations applied to T-S covariance. Also, in ODA<sub>111</sub>, since better physical balance between temperature and salinity is maintained, the assimilation is expected to extract the observational information more efficiently. Due to a substantial increase of data in the Southern Ocean and Indian Ocean from XBT to Argo, the estimated time tendency of heat content is improved greatly by ODA<sub>111</sub> (compare Figure 8f to Figure 8e). Particularly, ODA<sub>111</sub> eliminates the large errors at the entrance of the Labrador Sea in ODA<sub>110</sub>. Given the same reasonable coverage of temperature observations over the Northwest Atlantic region in both the 20th century XBT and 21st century Argo, the improvement of the temperature assimilation near the Labrador Sea should be attributed to the use of direct salinity observations in ODA<sub>111</sub>. The improved thermohaline structure must better the estimate of North Atlantic deep convection. In addition, it is noticed that owing to the Argo float's drift by the ocean currents (Figure 4), the Argo deploy contains relatively sparse observations over the eastern part of the North Atlantic subtropical gyre. This also creates errors for the time tendency of the North Atlantic temperature in ODA<sub>111</sub>. The sensitivity of the estimated time tendency of the North Atlantic temperature to the density of observations in this area may be associated with the strong temperature gradient across the North Atlantic subtropical gyre (e.g., see Figure 8b). This also needs to be further explored in the future studies.

#### 4. Detection of Salinity Variability

[36] Given that the 20th century XBT provides temperature observations only, this section attempts to answer: (1) How much of salinity variability can be rebuilt by applying temperature observations to the model-provided T-S covariance? (2) With the direct salinity observation in the 21st century Argo network, how much does the assimilation improve the estimate of the interannual variability and decadal trend of salinity?

##### 4.1. Temperature Observations With a T-S Relationship

[37] This section analyzes and compares the assimilation results of salinity in ODA<sub>000</sub> and ODA<sub>100</sub> (Figure 9 and Table 3). Compared to the control simulation, NOAssim<sub>00</sub>, except for the North Atlantic, the salinity anomalies of both assimilations have a trend to approach the truth, but the convergent rate is much slower than the temperature anomalies (compare Figure 9 to Figure 5). Both assimilations reduce the salinity errors over the upper ocean greatly from NOAssim<sub>00</sub> for most of the basins and the World Ocean (46% for the Pacific and 23% for the World Ocean, for instance) (Table 3). There is almost no difference in salinity RMS errors between ODA<sub>000</sub> and ODA<sub>100</sub> except

for the Arctic Ocean where the error of ODA<sub>000</sub> is larger than ODA<sub>100</sub> (compare the ODA<sub>100</sub> column to the ODA<sub>000</sub> column). Although the salinity assimilation applying a T-S relationship to temperature observations appears a little more sensitive to the different setting of radiative forcings than temperature assimilation, consistent with the heat content results, in general, the use of the temporally varying GHGNA records does not make significant improvement on the estimate of the salinity variability within a 25 year assimilation period. The following analysis will show that applying the model-provided T-S covariance to temperature observations only makes the upper ocean salinity convergent mostly in the tropical ocean.

[38] In this coupled system, the salinity adjustment in ODA<sub>000</sub> and ODA<sub>100</sub> comes from two parts. One part is the direct projection from oceanic temperature observations by T-S covariance, and the other part is the response of the coupled model to the ODA-generated SSTs. For example, when the atmosphere is driven by the ODA-generated SSTs, the precipitation and surface wind stress alter the salinity distribution near the surface ocean. Eventually, the adjustment of the top ocean salinity is a combination of these two contributions while the changes of the salinity in deep ocean mainly rely on the response of oceanic circulations to the adjustment of the upper ocean. Generally, the significant salinity adjustment produced by the temperature observations through T-S covariance mainly occurs in the tropical ocean. In the tropics, the strong T-S relationship from active air-sea interactions (convective precipitation linked with warm SSTs) and the isopycnal nature of thermocline oscillations [Zhang *et al.*, 2007] are able to retrieve the variability of the top ocean salinity anomalies to some degree (Figure 10). In the extratropics and deep oceans, probably due to fresh water forcings and the impact of large-scale transport processes as well as the reduced XBT coverage, the adjustment based on local T-S covariance and temperature observations is insufficient to constrain the salinity. For example, the salinity assimilation in ODA<sub>000</sub> and ODA<sub>100</sub> produces a negative salinity time tendency (oceans continue to be freshened) in the top 2000 m in most of the basins and the World Ocean (Figure 11). However, clear attributions of these factors to salinity constraint requires further research work.

[39] A noticeable phenomenon in ODA<sub>000</sub> and ODA<sub>100</sub> is that negative anomalies of the World Ocean salinity overshoot the truth in the deep ocean (see Figure 6c). The ocean in these assimilations is too fresh and the Southern Ocean is the main contributor for the overshooting (Figure 6d). Here we can use the lines of temperature and salinity anomalies in NOAssim<sub>00</sub> and NOAssim<sub>11</sub> (dashed and solid green lines in Figures 5, 6b, 6d, and 9) as 2 ensemble members of the model ocean to roughly estimate how the assimilation model responds to upper ocean temperature observations to form the deep ocean's salinity anomalies. In the top 700 m of the Southern Ocean, the NOAssim<sub>00</sub> water is colder and saltier than NOAssim<sub>11</sub> (see dashed/solid green lines in Figures 5 and 9), while in the deep ocean, the NOAssim<sub>00</sub> water is colder and fresher than the NOAssim<sub>11</sub> (see dashed/solid green lines in Figures 6b and 6d). This indicates a negative correlation between the deep ocean's salinity and the upper ocean's temperature observations. It says that the assimilation model responds to the warming of the top

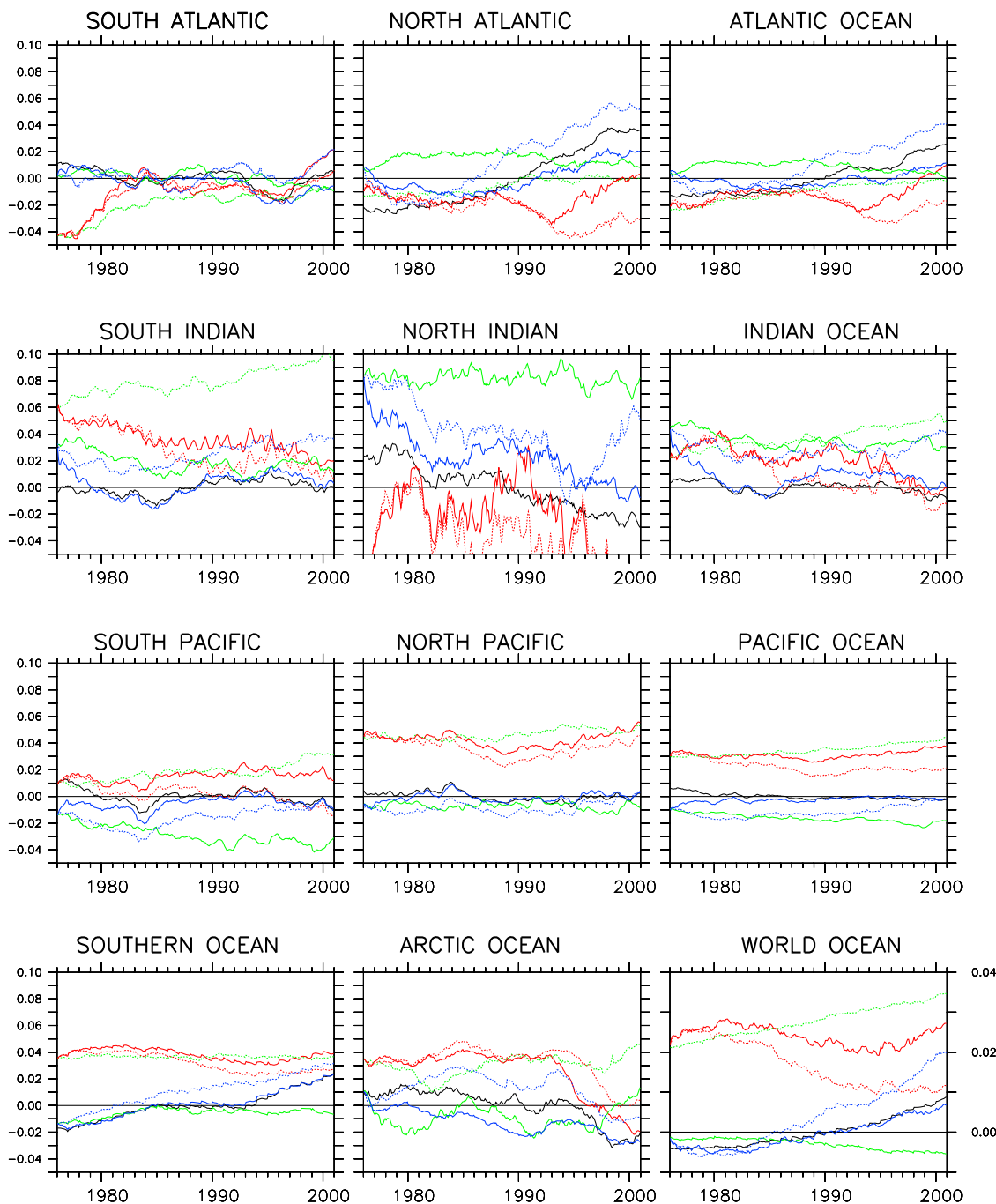


Figure 9. Same as Figure 5 but for the salinity.

ocean of the Southern Ocean by making the water fresher. During the last 10 years of the assimilation, the averaged T-S covariance in  $ODA_{000}$  (estimated by the Southern Ocean domain-averaged temperature and salinity over the top 2000 m) is  $-5 \times 10^{-5}$  psu  $^{\circ}C$ . Given a warming of  $0.25^{\circ}C$  and a temperature standard deviation of  $0.087^{\circ}C$ , regression produces a freshening of  $-1.5 \times 10^{-4}$  psu. The freshening rate is seriously underestimated by a domain average, but it does indicate a freshening trend. However, understanding the mechanism of the Southern Ocean’s freshening trend induced by a warming trend of the upper ocean requires further research work on the Southern

Ocean’s circulations (the Antarctic circumpolar circulation, for instance).

**4.2. Forced Oceanic ICs Versus Control Oceanic ICs**

[40] The salinity assimilation errors of  $ODA_{110}$  which uses the forced ICs are much smaller than the errors of  $ODA_{100}$  (compare the  $ODA_{110}$  column to the  $ODA_{100}$  column in Table 3, also compare dashed blue lines to red lines in Figures 9, 6c, and 6d). The biggest improvement from  $ODA_{100}$  to  $ODA_{110}$  is found in the Indian Ocean where the RMS error is reduced by 40% for the top 700 m and 50% for the top 2000 m. Generally, the improvement in

**Table 3.** RMS Errors of Salinity Over the Top 700 m During the Last 20 Years in Two Model Simulations and Four Assimilation Experiments<sup>a</sup>

Basin	NOAssim <sub>00</sub>	NOAssim <sub>11</sub>	ODA <sub>000</sub>	ODA <sub>100</sub>	ODA <sub>110</sub>	ODA <sub>111</sub>
SAT	0.10(-1)	0.15(0.2)	0.08/20(-0.4)	0.08/0(-0.1)	0.06/25(0.5)	0.05/17(-0.4)
NAT	0.14(-1)	0.24(1)	0.11/21(-3)	0.11/0(-2)	0.08/27(2)	0.09/-13(-0.5)
AT	0.13(-1)	0.22(0.6)	0.10/23(-2)	0.10/0(-1)	0.07/30(1)	0.07/0(-0.5)
SIN	0.15(8)	0.15(2)	0.14/7(2)	0.13/7(3)	0.08/38(3)	0.05/38(0.1)
NIN	0.19(-8)	0.22(9)	0.26/-37(-4)	0.26/0(-2)	0.17/35(4)	0.09/47(2)
IN	0.17(4)	0.18(3)	0.18/-6(0.7)	0.18/0(2)	0.11/39(3)	0.06/46(0.7)
SPC	0.10(2)	0.14(-3)	0.06/40(0.2)	0.06/0(2)	0.05/17(-1)	0.04/20(-0.3)
NPC	0.14(5)	0.16(-0.7)	0.08/43(4)	0.08/0(4)	0.05/38(-0.8)	0.04/20(0.05)
PC	0.13(4)	0.15(-2)	0.07/46(2)	0.07/0(3)	0.05/29(-1)	0.04/20(-0.1)
SO	0.08(3)	0.10(-0.8)	0.07/13(3)	0.07/0(3)	0.05/29(1)	0.03/40(0.1)
AO	0.12(3)	0.17(-0.6)	0.09/25(4)	0.06/33(3)	0.07/42(2)	0.06/14(-1)
WO	0.13(3)	0.16(-0.4)	0.10/23(1)	0.10/0(2)	0.07/30(0.5)	0.05/29(-0.1)

<sup>a</sup>RMS errors of salinity is given in psu. The RMS's reduction (%) of assimilation from the case to which it is compared (for ODA<sub>000</sub> the RMS's reduction is from NOAssim<sub>00</sub>, for ODA<sub>100</sub> the reduction is from ODA<sub>000</sub>, for ODA<sub>110</sub> the reduction is from ODA<sub>100</sub>, and for ODA<sub>111</sub> the reduction is from ODA<sub>110</sub>). The corresponding mean errors ( $10^{-2}$  psu) are listed in parentheses.

deep ocean is greater than in upper ocean (43% and 30% error reduction for the top 2000 m and top 700 m in the World Ocean, respectively). The improvement of salinity assimilation quality generated by the forced ICs is more than the improvement of temperature assimilation quality (for the top 700 m World Ocean, the error reduction is 30% for salinity and 23% for temperature, for instance). In addition, comparing the errors of the 2 decade salinity time tendency in ODA<sub>110</sub> (Figure 11e) and ODA<sub>100</sub> (Figure 11d), we found that the salinity tendency error of ODA<sub>110</sub> is smaller in the Atlantic and Indian Oceans.

[41] The analyses of heat content assimilation in section 3.2 have shown that due to the low-frequency nature of oceanic circulations the initial shocks have a serious impact on oceanic assimilation skill. Applying the model T-S relationship to temperature observations is a weak constraint for salinity, and the salinity assimilation therefore relies on the initial conditions more than the temperature assimilation. Thus, the use of the oceanic initial conditions that have the knowledge of long time temporally varying

radiative forcings is very important to obtain a relatively small assimilation error for salinity.

#### 4.3. Assimilation of Direct Salinity Observations

[42] When the direct salinity observations provided by the 21st century Argo are used, ODA<sub>111</sub> greatly reduces the mean and RMS errors of the salinity (solid blue lines in Figures 9, 6c, and 6d, the ODA<sub>111</sub> column in Table 3) for most of the basins and the World Ocean from ODA<sub>110</sub>. In the North Atlantic Ocean, while the mean error is improved considerably, the domain-averaged RMS error increases. The salinity anomalies of the top 700 m in ODA<sub>111</sub> capture the truth variability very well after the spin-up of a few years. The assimilation also tends to reconstruct the truth variability of salinity anomalies in the top 2000 m ocean but with a much longer time scale. However, a noticeable separation between the salinity anomalies of ODA<sub>111</sub> and the truth still exist in the Indian and Arctic Oceans. It is also noticed that after 20 years the variability of the Arctic Ocean's salinity anomaly begins to follow the truth. This,

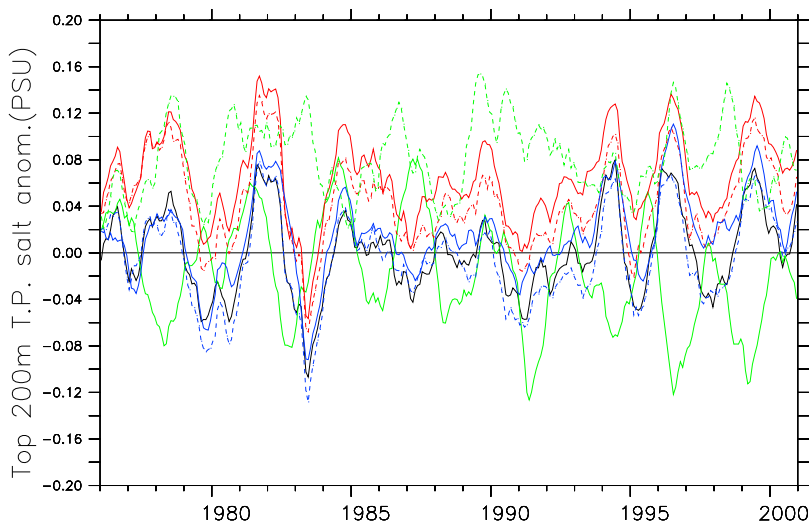


**Figure 10.** Time series of salinity anomalies averaged at the tropical Pacific ( $5^{\circ}\text{S}$ – $5^{\circ}\text{N}$ ) over the top 200 m in the truth (black line), two control free model simulations (dashed green line for NOAssim<sub>00</sub> and solid green line for NOAssim<sub>11</sub>), and four ODA experiments: ODA<sub>000</sub> (dashed red line), ODA<sub>100</sub> (solid red line), ODA<sub>110</sub> (dashed blue line), and ODA<sub>111</sub> (solid blue line).

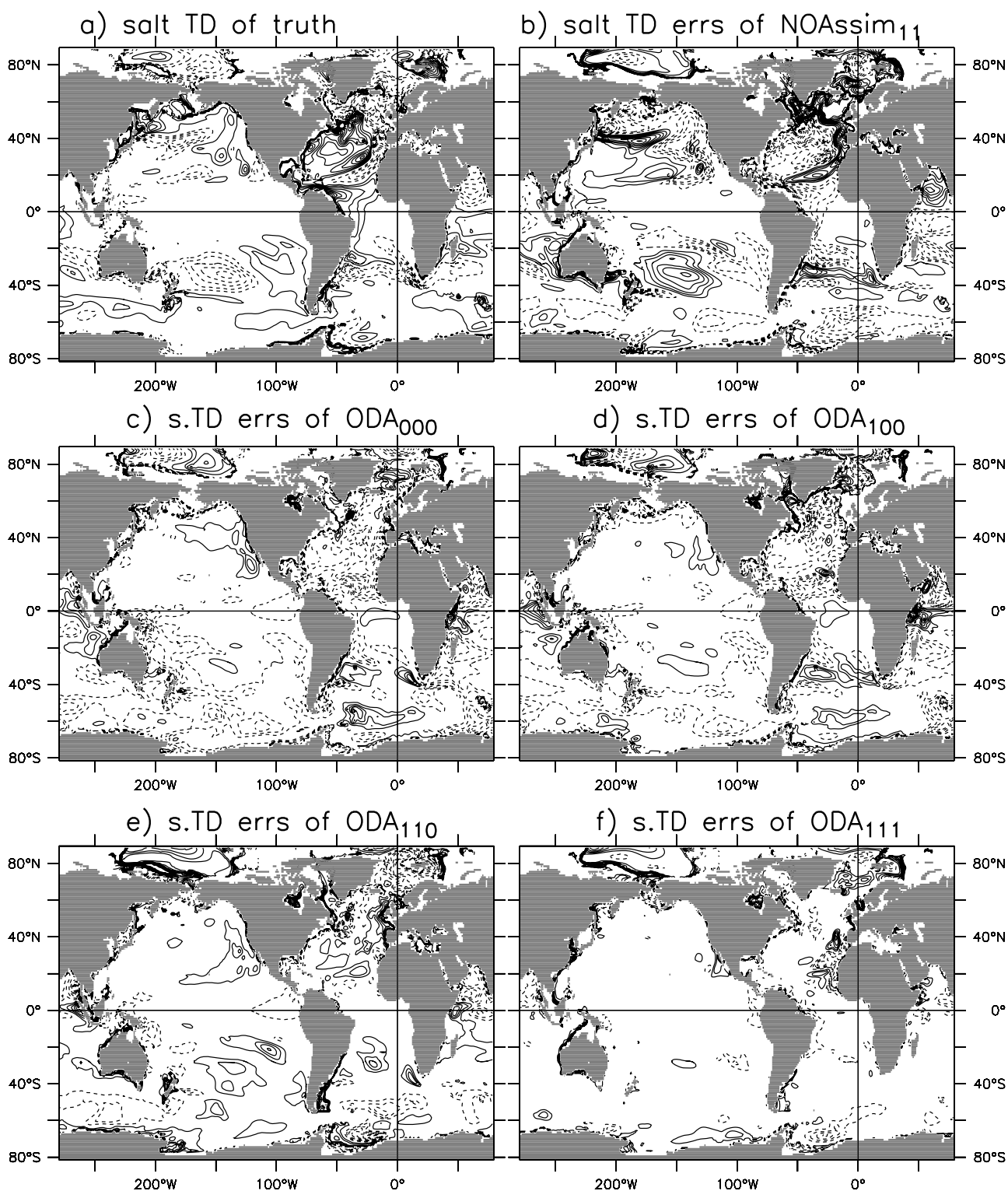


**Figure 11.** Same as Figure 8 but for the salinity of the top 2000 m and the contour interval is 0.01 psu.

again, can be explained by the slow response of the Arctic Ocean to the data constraints in the neighboring oceans as well as coupling effects in the system. Relatively large assimilation errors of salinity in the North Indian Ocean, again, is related to its sensitivity to the Indian monsoon system and the influence of through flows on the salt budget of the basin. In addition, the larger salinity RMS errors in

the North Atlantic Ocean in ODA<sub>111</sub> may be associated with the enriched spectrum of the overturning there, which will be discussed more in section 5.

[43] Oceanic assimilation results constrained by both the temperature and salinity observations can be viewed as an equilibrium of the oceanic state in which the oceanic data constraint is balanced by the surface forcings such as the

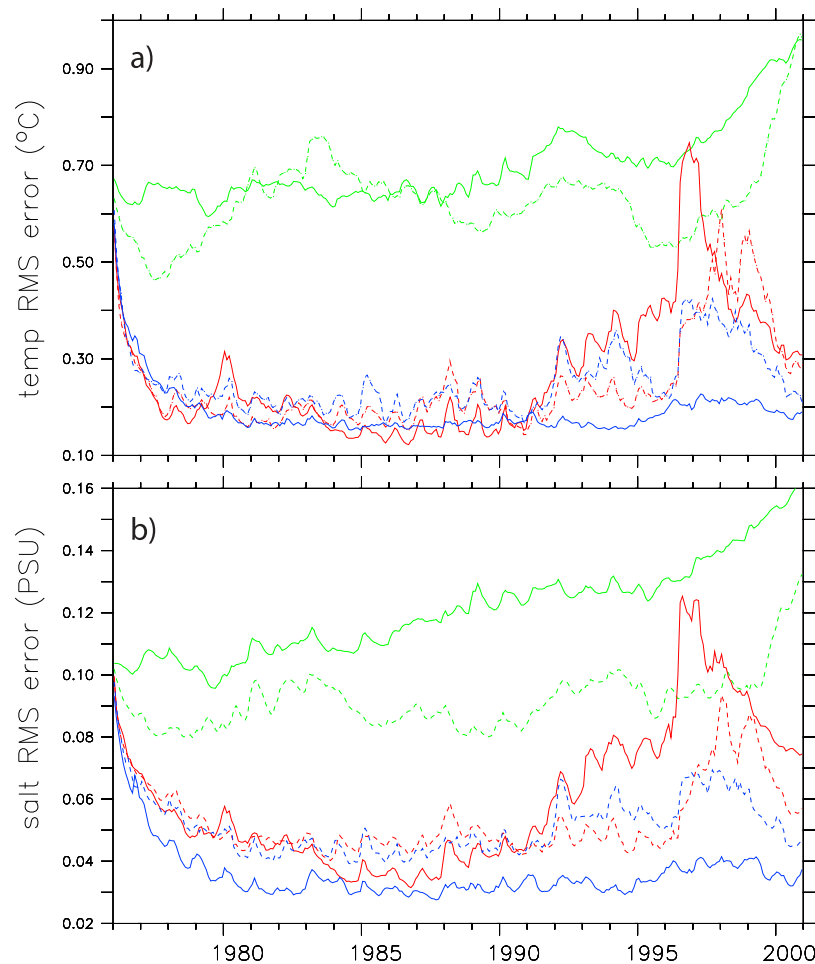


**Figure 12.** Time series of the RMS errors of oceanic (a) temperature and (b) salinity, computed in the top 2000 m North Atlantic Ocean ( $20^{\circ}$ – $70^{\circ}$ N) in ODA<sub>000</sub> (dashed red line), ODA<sub>100</sub> (solid red line), ODA<sub>110</sub> (dashed blue line), and ODA<sub>111</sub> (solid blue line). The RMS errors of NOAssim<sub>00</sub> and NOAssim<sub>11</sub> are plotted by dashed and solid green lines, respectively, as the reference for assimilation evaluation.

wind stress, heat and water fluxes from the atmosphere. By improving surface forcings of the ocean, preliminary results of a new coupled data assimilation experiment that includes both atmospheric and oceanic data assimilation components have shown an improved estimate of oceanic states [Zhang *et al.*, 2008]. This may be particularly true for such Oceans as the North Indian and Atlantic where oceanic circulations are more sensitive to the atmospheric forcings. However the complete examination of the impact of atmospheric data constraint on ocean state estimation needs to be done for further understanding.

## 5. Thermohaline Structure of the North Atlantic Ocean

[44] The North Atlantic (NA) thermohaline circulation (THC) has been recognized as one of the most important oceanic circulations to impact the global climate [e.g., Latif *et al.*, 2004; Zhang *et al.*, 2006]. The detection of the NA thermohaline structure by an oceanic observing system could serve as the first step for the NA THC estimation using real instrumental data (including oceanic and atmo-

spheric measurements). Also, initialization using the estimated oceanic conditions might be beneficial for the prediction of the NA THC. This section expands the analysis of the assimilation quality of ODA<sub>000</sub>, ODA<sub>100</sub>, ODA<sub>110</sub> and ODA<sub>111</sub> for the North Atlantic Ocean and highlights the impact of an oceanic observing system on the estimate of the NA thermohaline structure.

[45] First, we check the convergence of the assimilation temperature and salinity. Figure 12 presents the time series of RMS errors of the temperature and salinity in the upper 2000 m NA domain. Compared to the NOAssim<sub>00</sub> and NOAssim<sub>11</sub>, the assimilation errors for both temperature and salinity in all assimilations are substantially reduced during the first 15 years, but only ODA<sub>111</sub> shows a stable convergence after that. Further diagnoses reveal that the deep convection in the North Atlantic Ocean encounters a weak-to-strong regime transition during the last 10 years. Due to the existence of the deep convection, the T-S relationship governed by the oscillations of isopycnal surfaces could play an important role in salinity assimilation, which could somewhat help reconstruct the NA thermohaline structure. This conveys some hope for estimating the

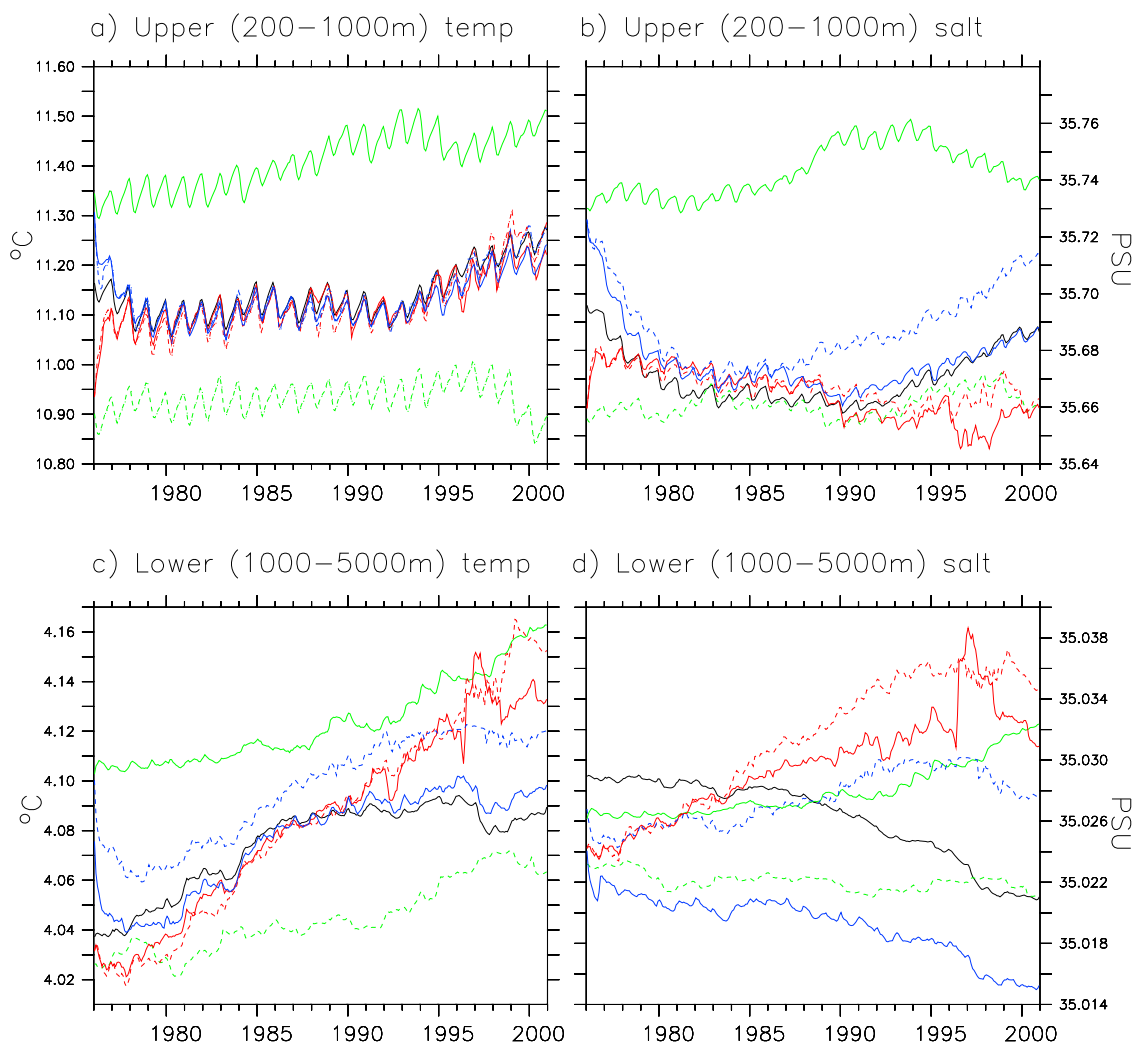


**Figure 13.** Time series of the domain-averaged oceanic (a and c) temperature and (b and d) salinity in the North Atlantic ( $20^{\circ}$ – $70^{\circ}$ N) over the upper (200–1000 m, Figures 13a and 13b) and lower (1000–5000 m, Figures 13c and 13d) portions of the North Atlantic thermohaline circulation.

NA THC using the 20th century XBT, as evidenced by the time series of the NA 200–1000 m temperature and salinity (red lines in Figures 13a and 13b), i.e., the assimilation using the 20th century XBT is able to rebuild the NA THC to some extent. However, all three assimilations that use the XBT observations show a sharp increase of temperature and salinity errors during the period of the THC regime transition (Figure 12). Corresponding jumps are also found in the time series of the estimated temperature and salinity of the NA deep ocean (Figures 13c and 13d). Considering relatively dense CTD and OSD temperature profiles available in the NA deep ocean, which are included in the 20th century network (Figure 3), results here suggest that the 20th century “XBT” fails to resolve the regime transition due to the lack of direct salinity observations. It is also observed that even in ODA<sub>111</sub> that uses the Argo temperature and salinity observations the deep ocean salinity (solid blue line) remains a separation from the truth although both share a multidecadal trend (Figure 13d).

[46] Reconstructing the NA thermohaline structure with a high accuracy is essential for estimating the variability of the NA THC. This is a complex and challenging task since

the NA THC is associated with multiple factors such as large-scale heat and salt transport in the NA domain, low-frequency NAO (North Atlantic oscillation) forcings from the atmosphere, fresh water forcings from sea ice and land runoff as well as their interaction with the local topographic features. The ODA experiments in this study have very weak constraints on the sea surface forcings from the atmosphere that freely responds to the ODA-generated SSTs. Given the strong linkage between the low-frequency NAO and the NA THC [Delworth and Greatbatch, 2000; Delworth and Dixon, 2000], a strong constraint on the sea surface forcings may improve the estimate of the NA THC. Preliminary results from a fully coupled assimilation experiment that adds an atmospheric data constraint into the coupled model has shown a considerable improvement on the estimate of the NA THC structure, which will be thoroughly examined in the extended studies.

## 6. Conclusions and Discussions

[47] Employing the ensemble coupled data assimilation system [Zhang *et al.*, 2007] to conduct oceanic data

assimilation (ODA) experiments, this study addresses the detection of oceanic variability. A perfect twin experiment framework is designed to assimilate the model-produced observations based on an existing oceanic observing system. The observations are produced by projecting an IPCC AR4 historical simulation [Randall *et al.*, 2007] onto the 20th century temperature and 21st century temperature and salinity observing system, superimposed by a white noise. These model-produced observations are assimilated into the same IPCC AR4 coupled model to examine the impact of temporally varying radiative forcings, oceanic initial conditions and oceanic observing systems.

[48] A series of ODA experiments have been done using the temporally varying or preindustrial fixed year greenhouse gas and natural aerosol radiative forcings, initial conditions spun up by historical or fixed year radiative forcings based on the 20th century ocean temperature or 21st century temperature and salinity network. Results established the following findings:

[49] 1. Within an assimilation period of a few decades, the adjustment of oceanic states is dominated by the data constraint imposed by the assimilated observations, while explicit knowledge of temporally varying GHGNA radiative forcings added to the model integration does not significantly impact on assimilation skill. This should not be surprising since the observations of the ocean already implicitly contain the information of temporally varying radiative forcings.

[50] 2. The initial conditions spun up by the temporally varying GHGNA radiative forcings reduce initial shocks for assimilation, especially in deep oceans. The small initial shock helps increase the effects of data constraint and the forced initial conditions produce therefore better assimilation skill than the control initial conditions spun up by the preindustrial fixed year (1860) GHGNA value. Given that both the 20th and 21st century *in situ* measurements do not provide observations below 2000 m (except for some deeper high-resolution CTD profiles), when numerical climate predictions are made, a long time assimilation spin-up for initialization may be necessary.

[51] 3. Both the 20th century XBT and 21st century Argo observing systems provide adequate sampling to capture the decadal/multidecadal trend and interannual variability of heat content. However, the salinity observations provided by the Argo system produce a significant improvement on the reconstruction of the thermohaline structure, indicating that the Argo system is very important for global oceanic climate studies.

[52] 4. In tropical oceans, the coupling mechanism produces a strong T-S correlation (e.g., the convective precipitation induced by a warmer SST freshens the surface near ocean). Thus, the salinity assimilation using temperature observations applied to T-S covariance captures the basic features of salinity variability. This conveys some hope that, when we use the 20th century instrumental XBT data to estimate the historical climate states, aided by the atmospheric data constraint, the use of T-S covariance may be able to capture some basic features of salinity variability in the tropics.

[53] As the first step of efforts to estimate the multi-decadal variability of oceanic climate, the obtained results from this perfect model study may be overly optimistic. The

ODA-generated variability resulting from data constraints in the presence of model bias contains both the data-sampled signal and bias-induced computational artifact [Segsneider *et al.*, 2000; Balmaseda, 2004; Vialard *et al.*, 2005; Balmaseda *et al.*, 2007]. To identify the computational artifact from the ODA-generated variability, in follow-up studies, we plan to perform imperfect twin experiments based on two CGCMs that are biased with respect to each other. In that way, we can explicitly define model bias, examine its impact on ODA, and seek potential solutions for the bias issue. On the other hand, the sea surface forcings in this study remain as free modes responding to the ODA-generated sea surface temperatures. This can restrict the efficacy of the oceanic data constraint. A fully coupled data assimilation experiment that includes both oceanic and atmospheric data constraints has shown an improvement on the estimate of oceanic states [Zhang *et al.*, 2007]. The correction of the surface forcings produced by the atmospheric data constraint in the fully coupled assimilation is expected to relax the oceanic model bias and thus improve the estimate of oceanic states. Primary estimates of coupled oceanic/atmospheric/sea ice/land states from 1980 to present have been done [Zhang *et al.*, 2008] by assimilating the instrumental data in the ocean and the NCEP/NCAR reanalysis of the atmosphere [Kalnay *et al.*, 1996] into the coupled model. Preliminary results from a set of retrospective one year ENSO (El Niño-Southern Oscillation) forecasts show a significantly improved skill over the old 3D-Var assimilation system. Refined versions of ECDA, which, for example, takes model bias correction into account, are expected to improve the estimates of the coupled states and enhance the accuracy of numerical climate predictions further. In order to widen the prior PDF and reduce model bias, a multimodel ensemble assimilation system which uses the GFDL's B grid (CM2.0) and finite volume (CM2.1) coupled models to compute error statistics for filtering analysis is under testing.

[54] In addition, in this study, we only use the *in situ* oceanic measurements. As an important part of the 21st century oceanic observing system, the satellite altimetric data contain integrated information of the vertical thermohaline structure and therefore the use of altimetric data is also expected to help relax the impact of model bias. How to use altimetric data to build the correlation structure to improve oceanic state estimation shall be an important aspect that will be explored in our next efforts.

[55] **Acknowledgments.** The authors would like to thank C. T. Gordon and Qian (Scott) Song, for their comments on earlier versions of this manuscript. Thanks go to Guijun Han for her suggestions in processing observation data during her visit at GFDL. Thanks also go to F. Zeng, Mike Spelman, Z. Liang, and H. Lee for their help on model configuration issue. The authors wish to express their special appreciation to Paul Nutkowitz in Princeton University who frequently provided suggestions on the presentation. The authors thank two anonymous reviewers for their thorough examination and comments that were very useful in improving the manuscript.

## References

- AchutaRao, K. M., B. D. Santer, P. J. Gleckler, K. E. Taylor, D. W. Pierce, T. P. Barnett, and T. M. L. Wigley (2006), Variability of ocean heat uptake: Reconciling observations and models, *J. Geophys. Res.*, *111*, C05019, doi:10.1029/2005JC003136.
- Anderson, J. L. (2003), A local least squares framework for ensemble filtering, *Mon. Weather Rev.*, *131*, 634–642.

- Balmaseda, M. A. (2004), Ocean data assimilation for seasonal forecasts, paper presented at Seminar on Recent Developments in Data Assimilation for Atmosphere and Ocean, Eur. Cent. for Medium-Range Weather Forecasts, 8–12 Sept.
- Balmaseda, M. A., D. Dee, A. Vidard, and D. T. Anderson (2007), A multivariate treatment of bias for sequential data assimilation: Application to the tropical oceans, *Q. J. R. Meteorol. Soc.*, *133*, 167–179.
- Carton, J. A., G. C. Chepurin, and X. Cao (2000), A simple ocean data assimilation analysis of the global upper ocean 1950–95. Part I: Methodology, *J. Phys. Oceanogr.*, *30*, 294–309.
- Collins, W. D., M. L. Blackman, G. B. Bonan, J. J. Hack, T. B. Henderson, J. T. Kiehl, W. G. Large, and D. S. McKenna (2006), The community climate system model version 3 (CCSM3), *J. Clim.*, *19*, 2122–2143.
- Delworth, T. L., and K. Dixon (2000), Implications of the recent trend in the Arctic/North Atlantic oscillation for the North Atlantic thermohaline circulation, *J. Clim.*, *13*, 3721–3727.
- Delworth, T. L., and R. J. Greatbatch (2000), Multidecadal thermohaline circulation variability driven by atmospheric surface flux forcing, *J. Clim.*, *13*, 1481–1495.
- Delworth, T. L., et al. (2006), GFDL CM2 global coupled climate models, part I: Formulation and simulation characteristics, *J. Clim.*, *19*(5), 643–674.
- Dee, J. (2005), Bias and data assimilation, *Q. J. R. Meteorol. Soc.*, *131*, 3323–3343.
- Dee, J., and A. M. da Silva (1998), Data assimilation in the presence of forecast bias, *Q. J. R. Meteorol. Soc.*, *124*, 269–295.
- Deser, C., and A. S. Phillips (2009), Atmospheric circulation trends, 1950–2000: The relative roles of sea surface temperature forcings and direct atmospheric radiative forcings, *J. Clim.*, *22*, 396–413.
- Forget, G., and C. Wunsch (2007), Estimated global hydrographic variability, *J. Phys. Oceanogr.*, *37*, 1997–2008.
- Geophysical Fluid Dynamics Laboratory Global Atmospheric Model Development Team (2004), The new GFDL global atmosphere and land model AM2/LM2: Evaluation with prescribed SST simulations, *J. Clim.*, *17*, 4641–4673.
- Gnanadesikan, A., et al. (2006), GFDL CM2 global coupled climate models, part II: The baseline ocean simulation, *J. Clim.*, *19*(5), 675–697.
- Griffies, S. M. (2005), Some ocean model fundamentals, in *Ocean Weather Forecasting: An Integrated View of Oceanography*, edited by E. P. Chassignet and J. Verron, pp. 19–74, Springer, Berlin.
- Griffies, S. M., et al. (2005), Formulation of an ocean model for global climate simulations, *Ocean Sci.*, *1*, 45–79.
- Hunke, E. C., and J. K. Dukowicz (1997), An elastic-viscous-plastic model for sea ice dynamics, *J. Phys. Oceanogr.*, *27*, 1849–1867.
- Kalnay, E., et al. (1996), The NCEP/NCAR 40-year reanalysis project, *Bull. Am. Meteorol. Soc.*, *77*, 437–471.
- Latif, M., et al. (2004), Reconstructing, monitoring, and predicting multidecadal-scale changes in the North Atlantic thermohaline circulation with sea surface temperature, *J. Clim.*, *17*, 1605–1614.
- Levitus, S., J. I. Antonov, T. P. Boyer, and C. Stephens (2000), Warming of the World Ocean, *Science*, *287*, 2225–2229.
- Levitus, S., J. I. Antonov, and T. P. Boyer (2005), Warming of the World Ocean, 1955–2003, *Geophys. Res. Lett.*, *32*, L02604, doi:10.1029/2004GL021592.
- Lock, A. P., A. R. Brown, M. R. Bush, G. M. Martin, and R. N. B. Smith (2000), A new boundary layer mixing scheme. Part I: Scheme description and single-column model tests, *Mon. Weather Rev.*, *128*, 3187–3199.
- Manabe, S. (1979), Effect of increasing the CO<sub>2</sub> concentration on the climate of a general circulation model, in *Carbon Dioxide Effects Research and Assessment Program: Workshop on the Global Effects of Carbon Dioxide from Fossil Fuels*, pp. 100–101, U.S. Dep. of Energy, Washington, D. C.
- Manabe, S., and R. J. Stouffer (1979), A CO<sub>2</sub>-climate sensitivity study with a mathematical model of the global climate, *Nature*, *282*(5738), 491–493.
- Moorthi, S., and M. J. Suarez (1992), Relaxed Arakawa-Schubert: A parameterization of moist convection for general circulation models, *Mon. Weather Rev.*, *120*, 978–1002.
- Randall, D. A., et al. (2007), Climate models and their evaluation, in *Climate Change 2007: The Physical Science Basis. Contribution of Working Group I to the Fourth Assessment Report of the Intergovernmental Panel on Climate Change*, edited by S. Solomon et al., chap. 8, pp. 589–662, Cambridge Univ. Press, Cambridge, U. K.
- Segsneider, J., M. Balmaseda, and D. L. T. Anderson (2000), Anomalous temperature and salinity variations in the tropical Atlantic: Possible causes and implications for the use of altimeter data, *Geophys. Res. Lett.*, *27*(15), 2281–2284.
- Stouffer, R. J., A. J. Weaver, and M. Eby (2004), A method for obtaining pre-twentieth century initial conditions for use in climate change studies, *Clim. Dyn.*, *23*, 327–339.
- Vidard, J., F. Vitart, M. A. Balmaseda, T. N. Stockdale, and D. L. T. Anderson (2005), An ensemble generation method for seasonal forecasting with an ocean-atmosphere coupled model, *Mon. Weather Rev.*, *131*, 1379–1395.
- Winton, M. (2000), A reformulated three-layer sea ice model, *J. Atmos. Oceanic Technol.*, *17*, 525–531.
- Wyman, B. L. (1996), A step-mountain coordinate general circulation model: Description and validation of medium-range forecasts, *Mon. Weather Rev.*, *124*, 102–121.
- Zhang, R., T. L. Delworth, and I. M. Held (2006), Can the Atlantic Ocean drive the observed multidecadal variability in Northern Hemisphere mean temperature?, *Geophys. Res. Lett.*, *34*, L02709, doi:10.1029/2006GL028683.
- Zhang, S., M. J. Harrison, A. Rosati, and A. T. Wittenberg (2007), System design and evaluation of coupled ensemble data assimilation for global oceanic climate studies, *Mon. Weather Rev.*, *135*, 3541–3564.
- Zhang, S., A. Rosati, M. Harrison, R. Gudgel, and W. Stern (2008), GFDL's coupled ensemble data assimilation system, 1980–2006 coupled reanalysis and its impact on ENSO forecasts, paper presented at 3rd International Conference on Reanalysis, World Clim. Res. Prog., Tokyo, 28 Jan. to 1 Feb.

M. J. Harrison, A. Rosati, and S. Zhang, Geophysical Fluid Dynamics Laboratory, Princeton University, PO Box 308, Princeton, NJ 08542, USA. (shaoqing.zhang@noaa.gov)